Concurrent SAR Imaging With F-Scan: Timing Design and Performance Prediction

João Pedro Turchetti Ribeiro, *Student Member, IEEE*, Thomas Kraus, Markus Bachmann, Renato Machado, *Senior Member, IEEE*, Gerhard Krieger, *Fellow, IEEE*, and Alberto Moreira, *Fellow, IEEE*

***Abstract*— The recently proposed frequency scanning (F-Scan) technique, together with the new International Telecommunication Union (ITU) allocation of 1200 MHz in X-band, enables the improvement of important performance parameters of synthetic aperture radar (SAR) acquisitions, such as the swath width, the signal-to-noise ratio, and the range ambiguity-to-signal ratio. The concurrent imaging technique, in turn, increases the flexibility of the radar system by allowing the simultaneous imaging of two or more areas with independent imaging modes. The integration of both techniques, therefore, enables the already valuable concurrent mode to achieve much better performance. Furthermore, motivated by the high-resolution wide-swath (HRWS) mission proposal in X-band, the displaced phase center antenna (DPCA) technique is considered to improve the azimuth resolution by using multiple receive (Rx) channels in azimuth. In this article, we discuss the design and performance of a new concurrent imaging mode that is enhanced by the F-Scan and DPCA techniques to make simultaneous imaging more flexible and powerful. Special attention is given to timing, range ambiguities, and availability aspects. The capability to simultaneously acquire two high-quality images with noteworthy flexibility is innovative and of great value, not only in daily operational applications but especially in extraordinary and crisis situations.**

***Index Terms*— Concurrent imaging, frequency scanning (F-Scan), high resolution, synthetic aperture radar (SAR), wide swath.**

I. Introduction

THE current generation of synthetic aperture radar (SAR) is capable of acquiring radar images with very high resolution through spotlight (ST) modes [1], [2] and also very wide swaths by employing either the ScanSAR or the terrain observation by progressive scans (TOPS) mode [3], [4], [5]. The long-established stripmap (SM) mode represents a trade-off between resolution and scene size of the previous modes [6]. To achieve more frequent observations of the whole Earth with high resolution, many new techniques are currently being proposed in the scientific community. The current generation of spaceborne systems, for instance, the Sentinel-1 mission, can interferometrically image the whole globe with a resolution of 5 × 20 m in range and azimuth, respectively, every 6 days when two operational satellites are in orbit [7].

One of the limitations of the traditional state-of-the-art imaging modes is the limited flexibility of adjusting the performance for different targets. For instance, it may be of interest to image two distinct areas separated far apart in range (a few hundred kilometers) with high resolution but with no need to image anything in between them. Alternatively, one could be interested in imaging specific buildings within a small area with high resolution but also simultaneously needing a broad view with a lower resolution requirement of the surrounding area. Such applications currently require multiple overflies. This leads to time delays between the acquisitions of several days in the spaceborne case [8]. This delay can be diminished by deploying multiple satellites in the same orbital plane to reduce the effective repeat cycle [9]. An interesting alternative was introduced in [10] and [11], in which a concurrent imaging technique was proposed to acquire multiple SM swaths simultaneously. This idea was then further developed in [12], [13], [14], and [15] and experimentally demonstrated with the German X-band satellite TerraSAR-X (TSX). The increased flexibility was indeed achieved, but at the cost of imaging performance, namely worse ambiguity ratios and swath widths.

Currently, many studies can be found in the literature proposing improvements to SAR systems by means of digital beamforming (DBF) in elevation [16], [17], [18]. DBF systems are, however, complex and hard to realize within restricted budgetary constraints. For X-band systems, a cost-effective alternative to DBF has been proposed for use in upcoming missions [19]. Taking advantage of the new International Telecommunication Union (ITU) allocation of 1200 MHz in the X-band, the frequency scanning (F-Scan) technique was introduced for the first time in [20], [21], and [22]. F-Scan consists of an analog beamforming technique to achieve a frequency-dependent beam steering in elevation that can be implemented with much less hardware complexity than DBF. Besides being more affordable, F-Scan also brings improvements in terms of signal-to-noise ratio (SNR), swath width, and peak power requirements. It was, therefore, an important development in SAR technology. The design and performance prediction of F-Scan acquisitions are investigated in [23] and [24]. Further investigations focusing on the signal modeling and processing approaches have been published in [25] and [26].

F-Scan improves primarily the performance in range. In azimuth, in turn, the displaced phase center antenna (DPCA)

Manuscript received 22 November 2023; revised 26 March 2024 and 17 May 2024; accepted 9 July 2024. Date of publication 17 July 2024; date of current version 1 August 2024. *(Corresponding author: João Pedro Turchetti Ribeiro.)*

João Pedro Turchetti Ribeiro, Thomas Kraus, Markus Bachmann, Gerhard Krieger, and Alberto Moreira are with the Microwaves and Radar Institute, German Aerospace Center (DLR), 82234 Weßling, Germany (e-mail: joao.turchettiribeiro@dlr.de).

Renato Machado is with the Department of Telecommunications, Aeronautics Institute of Technology (ITA), São José dos Campos 12228-900, Brazil.

Digital Object Identifier 10.1109/TGRS.2024.3430084

technique was proposed as a way to lighten the well-known trade-off between azimuth resolution and swath width originating from the restrictions in the pulse repetition frequency (PRF) selection [3], [27]. The technique exploits an antenna that can be split into independent along-track channels during radar echo reception to increase the number of acquired azimuth samples. By tailoring the antenna size and the number of channels, both the azimuth resolution and the swath width can be improved beyond the traditional limit of single-channel systems at the cost of an increased data volume to be transmitted to the ground.

The article at hand refers to the development of a concurrent imaging mode with not only significant flexibility but also very high performance in the context of the HRWS mission proposal [19], [28], [29]. By combining and adapting individual techniques previously introduced in the literature, a novel, concurrent imaging mode is proposed here. The objective is to acquire two images, for instance, two SM scenes at different regions, one SM and one ST at independent positions, or two STs over different areas of interest. Such a technique would enhance the capabilities of the HRWS mission by adding high-performance concurrent imaging to its portfolio of imaging modes. The combined use of F-Scan and DPCA is expected to improve the previous drawbacks of limited swath width and compromised ambiguity performance of the concurrent imaging mode. This combination is considered an attractive, cost-effective concept for future HRWS SAR missions in X- or Ka-band [23], [28]. This article addresses the idea from theoretical and simulation points of view, as such a radar system is not yet operationally available. However, it has already been considered for future SAR missions [28], [30].

The article is structured as follows. Section II presents the imaging technique, describing the basic concept and an exemplary design of the novel imaging mode. In Section III, the method to evaluate its performance is developed, highlighting the differences from traditional imaging modes. Section IV extrapolates the previous two sections to a global context, assessing the timing and performance for a large variety of acquisition scenarios. Strategies for further optimization and improvement are described in Section V. Finally, Section VI concludes the article, summarizing the main outcome and findings of the work.

II. Imaging Mode Concept

A. F-Scan Imaging Concept

Traditional imaging modes transmit a wide beam toward the whole imaged scene in range direction. Consequently, every target on the ground is illuminated with the total signal bandwidth. The effective antenna aperture is adjusted by either phase spoiling or by artificially reducing the antenna size to achieve a beam with the demanded scene width. This approach, however, results in lower antenna gains, affecting the SNR performance. To counter this issue, wide-swath imaging techniques sacrifice azimuth resolution instead. This can be achieved, for instance, by illuminating different elevation angles in a sequence of bursts (e.g., ScanSAR and TOPS).

F-Scan was introduced as a way to increase the swath width of SAR acquisitions by using, counterintuitively, a narrow pencil beam in elevation that changes its direction as a function of the frequency of the transmitted pulse. The pencil beam sweeps over the target area both on transmit (Tx) and receive (Rx), spreading the total bandwidth across the scene. In contrast to the azimuth resolution trade-off of ScanSAR, the degradation involved in F-Scan is the range resolution. This resolution loss is a consequence of the total bandwidth being spread across the scene, thus reducing the effective bandwidth of each individual point target. Moreover, the wider the scene is compared to the beamwidth, the lower the resolution achieved. Consequently, implementing F-Scan is more convenient in higher frequency bands, such as the X- and Ka-band, where wider bandwidths are available to compensate for the bandwidth spread. The analysis of an F-Scan acquisition and the design of concurrent acquisitions making use of it are described in this section.

The central idea of F-Scan is to start the transmission pointing toward the far edge of the scene, and then progressively scanning toward the near range. This scanning is achieved in frequency through analog beamforming by making use of phase shifters (PSs) and true time delay lines (TTDLs) [20]. For each acquisition, the PSs and TTDLs are adjusted so that the antenna is pointing toward the far edge for the first transmitted frequency (ψ_f and f_f below), while for the last frequency the antenna is pointing to the near edge (ψ_n and f_n below). Considering planar phased array antennas, the required phase ramp δ and time delays $\Delta\tau$ between neighboring elements can be calculated by

$$\begin{cases} \delta = \dfrac{2\pi d}{c_0} \dfrac{(\sin\psi_\mathrm{f} - \sin\psi_\mathrm{n})}{\frac{1}{f_\mathrm{n}} - \frac{1}{f_\mathrm{f}}} & \text{(1a)} \\ \Delta\tau = \dfrac{d}{c_0}\left(\dfrac{f_\mathrm{f}\sin\psi_\mathrm{f} - f_\mathrm{n}\sin\psi_\mathrm{n}}{f_\mathrm{f} - f_\mathrm{n}}\right) & \text{(1b)} \end{cases}$$

where c_0 is the speed of light in free space, d the element spacing, f the Tx frequency, and ψ the antenna off-boresight angle in elevation [20], [31]. The subscripts "n" and "f" refer to the near and the far edges, respectively. The antenna off-boresight angle ψ is related to the imaging look angle β by the equation $\beta = \psi + 33.8°$, where 33.8° is the satellite roll angle assumed for the system considered in this investigation. Additionally, this formulation encompasses the use of both up- and down-chirp waveforms. Thus, for a toggling operation of up and down chirps, which will be shown to be of interest in Section II-E, the antenna needs to reconfigure its PSs and time delay lines from pulse to pulse.

The Tx scheme is a combination of the time, frequency, and look angle domains. For an F-Scan transmission using an up chirp, the relation between these domains is depicted in Fig. 1. The look angles β_f and β_n represent the pointing of the antenna at the beginning (to the far range) and end (to the near range) of the transmission, respectively. Additionally, B_t is the total Tx bandwidth, τ_p the pulse duration, and f_c the center frequency. In F-Scan acquisitions, a target is only considered to be fully imaged if it is scanned by the whole half-power beamwidth of the antenna pattern in elevation ($\mathrm{HPBW_{el}}$). For instance, the targets at β_f and β_n are scanned only by half of the $\mathrm{HPBW_{el}}$. Consequently, they are considered not to be part of the final scene. The effectively imaged area is highlighted by the green line in Fig. 1. The boundaries in range of the final image are defined by the effective look angles $\beta_\mathrm{f,eff}$ and $\beta_\mathrm{n,eff}$.

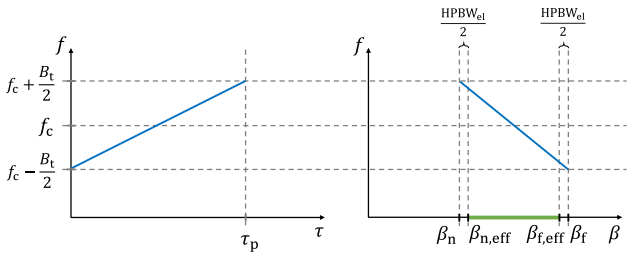

Fig. 1. F-Scan instantaneous Tx frequency in terms of (left) fast time and (right) look angle. The look angle refers to the pointing of the peak of the main lobe.

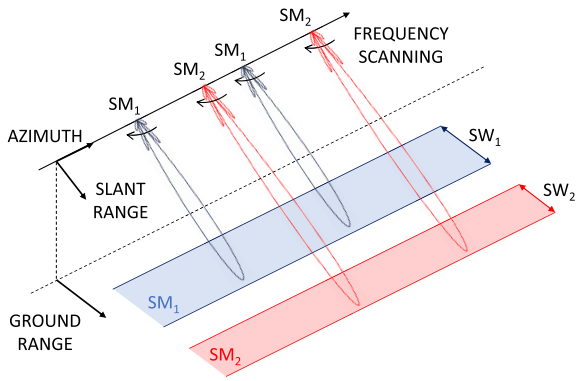

Fig. 2. Schematic representation of the novel imaging technique. It allows the simultaneous acquisition of two images with independent modes combining F-Scan with the concurrent imaging technique. In this example, two simultaneous acquisitions in SM mode are shown.

The idea of such scanning, as first introduced in [17] by the name of intrapulse beam steering in elevation, is to compensate for the different echo delays of the swath by the Tx pulse duration. It is possible, therefore, to determine a specific pulse duration so that echoes from near and far ranges arrive simultaneously at the antenna. In the context of F-Scan, this specific scheme is called the fully overlapped scenario [32]. For arbitrary pulse durations, some echo compression is still present, i.e., the echoes from the whole swath can be received in a shorter duration than with the traditional SM mode. This compression of the echoes in time can be used to increase the efficiency of the time-domain usage, i.e., increase the swath width for a given PRF (relative to conventional SM acquisitions), but at the cost of degraded range resolution.

B. Basic Concept of Concurrent F-Scan Imaging

The concurrent imaging technique, in turn, is the interleaving of the Tx pulses of two different modes from pulse to pulse. Its integration with F-Scan is straightforward. For instance, one could consider a concurrent SM/SM imaging, in which the transmission to both scenes occurs with F-Scan. This exemplary scenario is visualized in Fig. 2. To allow more flexibility to better tailor the performance parameters, each imaging mode can employ independent pulse durations, duty cycles, and Rx echo windows, as introduced in [14]. Such degrees of freedom reduce the minimum distance between the swaths and allow a finer adjustment of the scenes' swath widths and noise-equivalent sigma zero (NESZ). Additionally, as in (1), two pairs of phase shifts and time delays are obtained and toggled from pulse to pulse to guarantee the correct antenna pointing for each scene.

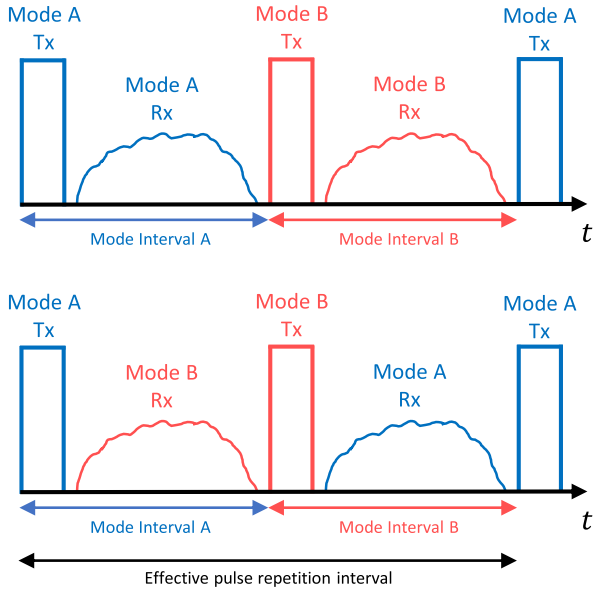

Fig. 3. Schematic visualization of the possibilities for the Tx and Rx events of the concurrent imaging considered in this research. Due to the long distance between the satellite and ground, the received echoes were transmitted many pulses before, such that the Rx echoes in the figure are not referent to the Tx pulses shown.

Fig. 2 depicts an SM/SM scenario, but interleaving with an ST mode is also possible. In general, the two images can be two SM scenes at different regions, one SM and one ST at independent (even overlapping) positions, or two STs over different areas of interest. The decision to use F-Scan in the ST acquisitions depends on the desired swath width. Typically, only a small patch is targeted so that the antenna beamwidth is already enough to cover the whole scene, and F-Scan is not required. In these situations, even if F-Scan is not considered, the ST mode still benefits from the high-gain pencil beam in terms of improved NESZ and range ambiguity performance.

An additional visualization of the concurrent mode is depicted in Fig. 3. It shows the possibilities for the Tx and Rx events of two generic modes denoted A and B in the time domain. It is highlighted that the echoes of each mode can be received either before or after the Tx pulses of the respective mode. This possibility brings extra flexibility in the positioning of the two scenes. A further alternative for concurrent imaging is to have both transmissions in sequence, followed by both receiving echo windows. This alternative, however, is not considered in this investigation.

C. System Description

The system considered in this work is the German X-band mission proposal HRWS [19], [28], [29]. Its center frequency is 9.8 GHz with a total bandwidth of 1200 MHz. The antenna has a total area of 8.4 m^2, with 6.0 m in azimuth and 1.4 m in elevation. Additionally, the duty cycle is limited to a maximum of 30%, and the waveform considered is a linear frequency-modulated (LFM) chirp. The system parameters are summarized in Table I. They serve as the basis for the design and performance assessment of the imaging scheme described in this article.

Moreover, DBF in azimuth is also considered through the DPCA—also known as multiple azimuth phase centers

TABLE I
SYSTEM PARAMETERS

System Parameter	Value
Center frequency	9.8 GHz
Bandwidth	1200 MHz
Orbit height	514 km (LEO)
Antenna height	1.4 m (64 elements)
Antenna length	6.0 m (12 elements) - 4 channels
Maximum Duty Cycle	30 %
Waveform	Linear frequency-modulated chirp

(MAPS)—approach. The idea of DPCA is to employ a large Rx antenna in azimuth and split it into N individual RF chains, while a single Tx phase center is maintained [27], [33]. This article considers a four-channel system. The potential improvement of the azimuth resolution by a factor of four comes along with the acquisition of four times more data, posing a tougher requirement in terms of the downlink capacity of the system.

To ensure a uniform sampling with DPCA, the PRF has to be chosen in such a way that the platform moves exactly half the antenna length between consecutive receptions. Using all four channels, this restriction is respected by employing an effective target PRF of

$$\mathrm{PRF}_{\text{eff, DPCA}}^{\text{4-ch}} = \frac{2\,v_s}{L_a} = 2560\ \text{Hz} \tag{2}$$

where v_s is the platform speed and L_a the antenna length in azimuth. Alternatively, by disregarding the first or the last phase center and using only three channels, the same effective sampling would be achieved with $\mathrm{PRF}_{\text{eff, DPCA}}^{\text{3-ch}} = 2\ v_s/L_a^{\text{3-ch}} = 3413.3$ Hz. Accordingly, the next PRF opportunities would be 5120 and 10 240 Hz, but these are not considered here, as the achieved swath width would be strongly limited.

In practical applications, these specific PRFs may not always be suitable, i.e., they may lead to nadir or Tx interference. This requires looking for PRFs in the vicinity of the target ones. Such PRF deviations lead to a nonuniform sampling, requiring, therefore, a signal reconstruction technique to return the data to a uniform grid [34]. To limit the negative effects of such a nonuniform sampling, in this work, the PRF range when DPCA is considered is limited, taking into account both the noise scaling and the azimuth ambiguity performance.

D. F-Scan Timing Assessment

The timing analysis serves as the basis for the determination of a fitting PRF in the design of SAR acquisitions. In this article, the terrain is assumed to be flat, and local topography is not considered. First, some conditions have to be fulfilled in the timing selection, such as avoiding nadir and Tx interference and obtaining the required swath width. Then, after the possible PRF ranges have been identified, a more detailed performance analysis is carried out to select the most suitable option.

An important factor to be considered in F-Scan acquisitions is the illumination duration of each target on the ground during the transmission scanning. This parameter is defined as the dwell time in [23] and can be calculated from the Tx pulse duration by

$$\tau_{\text{dwell}} = \frac{\mathrm{HPBW}_{\text{el}}}{\beta_{\text{f}} - \beta_{\text{n}}}\,\tau_{\text{p}}. \tag{3}$$

In the beginning of the transmission, it is clear that the far-range targets start to be imaged by the main lobe of the antenna pattern. From the equation above, it can be straightforwardly derived that the targets at near range start to be imaged after $\tau_{\text{p}} - \tau_{\text{dwell}}$. Consequently, considering linear scanning, one can derive that a target at a look angle β starts to be imaged by the leading edge of the antenna at the instant given by

$$\tau_{\text{lead}}(\beta) = \frac{\beta_{\text{f,eff}} - \beta}{\beta_{\text{f,eff}} - \beta_{\text{n,eff}}}\,(\tau_{\text{p}} - \tau_{\text{dwell}}) \quad \forall\,\beta \in [\beta_{\text{n,eff}}, \beta_{\text{f,eff}}] \tag{4}$$

with the subscripts "n, eff" and "f, eff" referring to the effective near and far ranges, respectively, as depicted in Fig. 1.

After the signal is transmitted, the determination of the round-trip delay is a matter of modeling the Earth's surface. For instance, assuming a spherical Earth, the distance between the platform and the target can be calculated by

$$R(\beta) = \frac{\sin\left\{\sin^{-1}\left[\left(1 + \frac{H}{R_{\text{e}}}\right)\sin\beta\right] - \beta\right\}}{\sin\beta} R_{\text{e}} \tag{5}$$

where R_{e} is the Earth radius and H the platform's height.

Regardless of whether a spherical, ellipsoidal, or any other model of the Earth's surface is considered, the echo delay is derived from the slant range by $\tau_{\text{delay}}(\beta) = 2R(\beta)/c_0$. It follows that the echoes from look angle β arrive at the antenna after the beginning of the transmission at the instant $\tau_{\text{rx,arrival}}(\beta) = \tau_{\text{lead}}(\beta) + \tau_{\text{delay}}(\beta)$.

For the fully overlapped scenario, the acquisition is designed such that the same arrival time is obtained for the near and far edges of the scene, i.e., the different echo delays are compensated by the Tx pulse duration. The required pulse duration to achieve such a condition is then

$$\tau_0 = \frac{2}{c_0}\,(R_{\text{f,eff}} - R_{\text{n,eff}})\,\frac{\beta_{\text{f}} - \beta_{\text{n}}}{\beta_{\text{f,eff}} - \beta_{\text{n,eff}}}. \tag{6}$$

As frequency is an inherent aspect of F-Scan, instead of the typical time by amplitude timing analysis, such acquisitions are better analyzed in the time–frequency domain. For an exemplary fully overlapped acquisition, the echoes received can be visualized as shown in Fig. 4. The figure summarizes the timing analysis, allowing one to know exactly when the echoes arrive and, moreover, with which frequencies. The fully overlapped aspect is clearly observable, as the echoes from the far (starting frequency −600 MHz) and the near range (starting frequency at around 214 MHz) arrive simultaneously. The area in gray ("RX Data") represents the echoes received with sufficient power, i.e., within the $\mathrm{HPBW}_{\text{el}}$ of the antenna pattern. Similarly, the arrival of the echoes depicted by the blue line can be seen as the leading edge of the pattern ("RX Pulse Start"), while the orange line as the lagging edge ("RX Pulse End"). Such visualization is key in the determination of a proper PRF for concurrent F-Scan acquisitions as will be discussed in the following section.

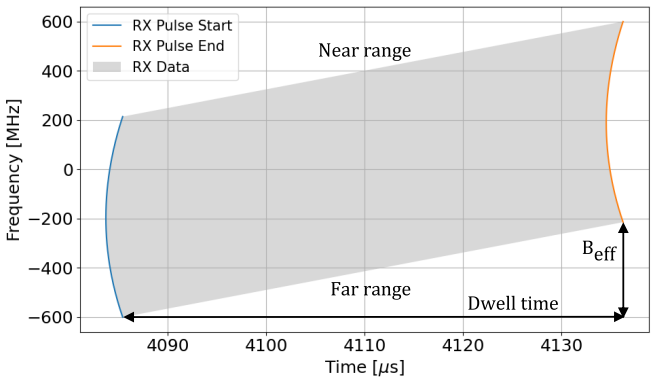

Fig. 4. Schematic representation of the received F-Scan echoes in the time–frequency domain. The image portrays a fully overlapped case in which targets from near and far edges arrive simultaneously. The scene in question is at an incidence angle of 31.50° and has a swath width of 30 km, while the Tx pulse duration is 158 μs. The echoes depicted refer to a Tx pulse starting at the instant zero so that the x-axis values display the round-trip delay. The effective bandwidth (B_{eff}) and the dwell time are also highlighted.

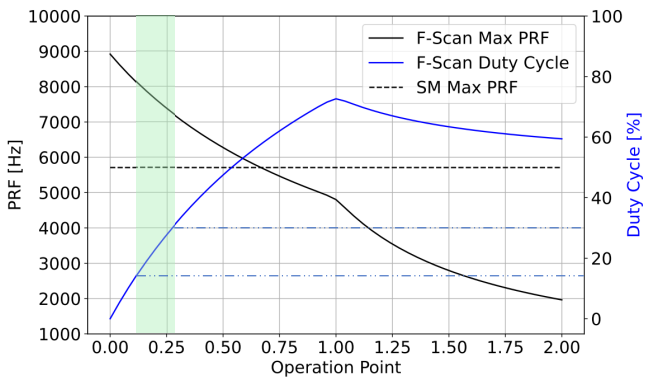

Fig. 5. Maximum PRF from a timing perspective of an F-Scan acquisition in comparison with a traditional SM one. The F-Scan pulse duration variation is represented on the x-axis. The green area represents F-Scan duty cycles between 15% and 30%.

Using a Tx pulse as in (6) leads to the behavior depicted in Fig. 4, where the echoes from near and far range arrive simultaneously. For the remaining scene, however, it can be seen that the echoes arrive slightly earlier. This effect is a consequence of transmitting a linear chirp toward the curved shape of the Earth. More generally, however, any other pulse duration can be considered. An interesting parameter that can be used to relate an arbitrary pulse duration to the one in (6) is the operation point [23], which is defined as $O_{\text{p}} = \tau_{\text{p}}/\tau_0$. Values smaller than unity mean that the echoes from near range arrive before those from far range. Conversely, values higher than unity represent an echo reversal, i.e., echoes from far range arrive first. The latter option is not convenient, as not only are longer pulse durations needed, but echo compression is also lost.

One of the main drawbacks of concurrent imaging is the limitation of the scene sizes. Therefore, it is of great interest to tailor the pulse duration of the F-Scan acquisition so as to increase the swath width for a given PRF. Even though the pulse duration corresponding to the fully overlapped scenario leads to the shortest Rx echo window, it is not the one achieving the widest swath, as very long Tx pulses are required for this. Simulating a 30 km scene at the incidence angle of 30°, Fig. 5 depicts the maximum possible PRF from a timing perspective for F-Scan (continuous black line) and for conventional SM (dashed black line). The antenna height considered for F-Scan is the one given in Table I. For different F-Scan operation points, the respective Tx pulse duty cycle is also depicted in blue. The conventional SM acquisition is assumed to use a duty cycle of 18%, which is typical for TSX SM acquisitions.

The fully overlapped case would be beneficial from the SNR or peak-to-average power ratio perspectives, as the duty cycle is maximized. However, for concurrent imaging, low operation points are more interesting because the time-domain usage efficiency is increased, i.e., higher PRFs can be used for the same swath width. Due to limited achievable peak power, the pulse duration cannot be too low to avoid strong SNR degradation. Combining this with the duty cycle system limitation as in Section II-C, the duty cycle of the transmission is restricted between 15% and 30% as highlighted by the green area in Fig. 5. The lower limit arises from the fact that it enables the imaging of wider swath widths and simultaneously limits the SNR degradation to −3 dB.

E. Concurrent Imaging Design

Concurrent acquisitions, as introduced in [12] and [14], benefit from having an extra degree of freedom from simultaneous imaging of two scenes. The interleaving of the modes in a pulse-to-pulse manner allows for the use of different pulse durations, duty cycles, and incidence angles. Consequently, each mode, when separately considered, is endowed with a different mode interval (MI). The MI, as visualized in Fig. 3, is defined as the interval from the beginning of the transmission of a mode until the end of the following Rx echo window. Due to the interleaving of the modes in concurrent acquisitions, the effective pulse repetition interval (PRI_{eff}) is simply the sum of the individual MIs. It follows for two generic modes A and B

$$\text{PRI}_{\text{eff}} = \text{MI}^{\text{A}} + \text{MI}^{\text{B}}. \tag{7}$$

The effective PRI is, therefore, the azimuth sampling interval, i.e., the duration between consecutive receptions of the same mode. Similarly, the effective PRF (PRF_{eff}) is defined as the inverse of the effective PRI. This value defines the azimuth sampling rate and, therefore, the azimuth resolution and ambiguity ratio.

The PRF determination from a timing perspective for traditional SM acquisitions is based on the timing/diamond diagram [6]. Such a graphical representation is neither feasible with F-Scan nor concurrent imaging, as the echo timings in F-Scan, for instance, directly depend on the pulse duration, the swath width, and the beamwidth. In concurrent acquisitions, the extra degrees of freedom also double the amount of parameters to be defined. These factors pose, therefore, an impediment to the determination of the PRF and the incidence angles on a 2-D visualization.

Due to this interrelation between the design variables in F-Scan, it is necessary to initially define input parameters. Namely, the swath widths and incidence angles of the areas of interest, as well as the duty cycle, are assumed to be predefined. The initial choice of duty cycle is tightly connected

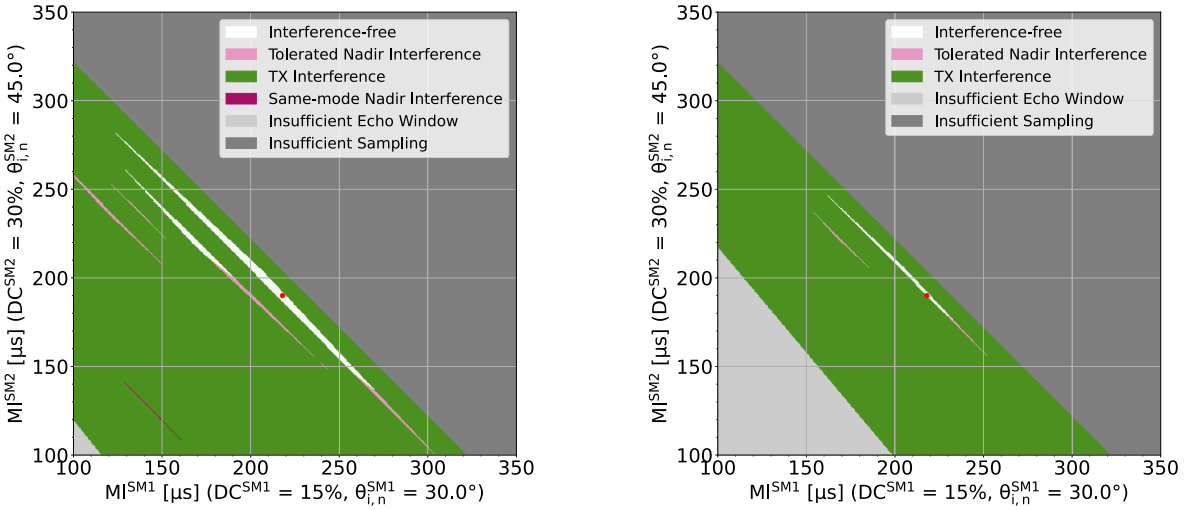

(a) 2x 20 km scenes. (b) 2x 30 km scenes.

Fig. 6. Interference maps for concurrent SM acquisitions 190 km apart with F-Scan. The available MI combination and the interference events are portrayed. (a) Two scenes with 20 km of swath width are considered; (b) swaths are increased to 30 km. The variable $\theta_{i,n}$ refers to the near-range incidence angle of the corresponding scene. The red dots highlight the MI combination of $\text{MI}^{\text{SM1}} = 218\ \mu\text{s}$ and $\text{MI}^{\text{SM2}} = 190\ \mu\text{s}$.

to the minimum NESZ requirement. Finally, the pulse duration of each mode is optimized to achieve a scenario free of both nadir and Tx interference.

On the one hand, Tx interference occurs when the antenna receives while transmitting. It must be avoided due to the high difference in power between the Tx signal and the received echoes. In monostatic systems, this power difference would saturate and may damage the receiver, not enabling the retrieval of the echoes.

Nadir interference, on the other hand, occurs when echoes coming from the ground straight below the satellite are received at the same time as the echoes from the imaged scene. This leads to a bright line in the final focused image, strongly disturbing its quality [35], [36]. In the concurrent mode, however, an important distinction must be made with respect to the nadir echoes. Due to the independence in design between the Tx pulses of the modes, different waveforms, pulse durations, and even bandwidths can be used. Therefore, same-mode nadir interferences must be differentiated from the corresponding cross-mode interferences. The latter represents the situation when the nadir echoes from the Tx pulse of one mode are received during the echo window of the other mode. Due to the recently published results demonstrating the feasibility of removing the nadir interference by waveform encoding, namely toggling up and down chirps on Tx [37], [38], one can assume the cross-mode nadir interference to be tolerable from a timing perspective.

In real applications, it is reasonable to assume that the areas to be imaged are well-defined, i.e., the scene sizes and incidence angles are previously known. Therefore, as a design example, let us consider a concurrent acquisition of two 20 km SM scenes, 190 km apart, one at an incidence angle of 30° and the other at 45°. The Tx duty cycles are 15% and 30%, respectively, chosen based on the discussion of Fig. 5. The remaining parameter to be defined is the pulse duration. At this point of the analysis, with F-Scan, imaged areas, and a given system, only the range resolution and the NESZ are already well-defined. Ambiguities and azimuth resolution, in turn, depend on the values chosen for the pulse duration. With the duty cycles predefined, the Tx pulse duration can also be seen as a function of the MI. Then, for combinations of MIs, Tx and nadir interferences are checked for both concurrent imaging modes. The visualization of such an analysis for the given example of two 20 km scenes is depicted on the left side of Fig. 6, while on the right the swath widths are increased to 30 km.

The interference map has the MIs on its axes and depicts the interference-free combinations in white, the cross-mode nadir interference in pink, the same-mode nadir interference in purple, and the Tx interference in green. Furthermore, the map also highlights restrictions in terms of insufficient sampling and insufficient Rx echo window. The dark gray area represents effective PRFs below 2370 Hz, which are ignored, as they would lead to degraded azimuth performance. The light gray area, in turn, represents the MIs that are too short to fit the received echoes. Therefore, the areas in gray are disregarded and do not need to be checked for interferences. Comparing the results for different swath widths on the left- and right-hand sides of Fig. 6, it is clear, and expected, that the timing availability decreases for wider swaths.

The white and pink areas—MI combinations allowing the acquisition from a timing perspective—are visibly small. However, only one combination is already sufficient to perform the acquisition. Naturally, the probability of finding such a combination strongly depends on the position and size of the scenes. In Section IV, the concept of availability rate will be discussed, which is a proxy for the likelihood of finding such a solution for a concurrent acquisition.

In both examples of Fig. 6, for instance, the highlighted combination (see red dot in Fig. 6) of $\text{MI}^{\text{SM1}} = 218\ \mu\text{s}$ and $\text{MI}^{\text{SM2}} = 190\ \mu\text{s}$ leads to an interference-free scenario. For this combination and the 30 km scenes, an additional step of optimization is performed. In order to make use of still unused time, the initial specified duty cycles are maximized. By increasing the duty cycles and, consequently, the duration of the Tx pulses, the required echo windows are reduced due

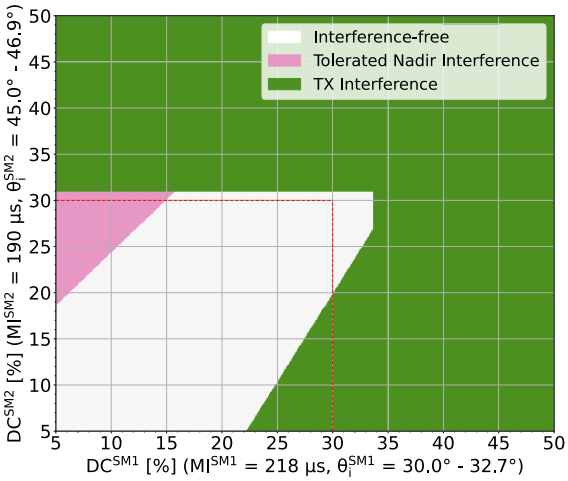

Fig. 7. Interference events obtained by varying the duty cycles of the modes. The scenes are 30 km in swath width, 190 km apart, with near-range incidence angles of 30° and 45°, and the MIs used are 218 and 190 μs, respectively. Such a visualization allows for the maximization of the initial duty cycle. The duty cycle limitation of 30% is highlighted by the dashed red line.

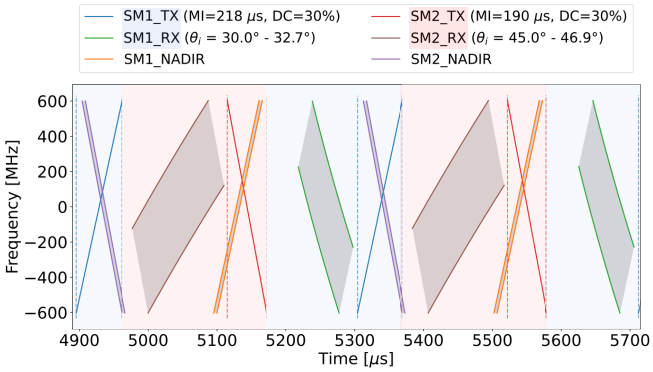

Fig. 8. Schematic time–frequency representation of the Tx and Rx events of an exemplary concurrent F-Scan acquisition with maximized duty cycles. This visualization highlights that little time is left unused, and also that no interference event is present in the acquisition. The vertical dotted lines separate transmission from reception and help to visualize that the echoes are not received during the transmission. Due to the long distance between the satellite and ground, the received echoes transmitted many pulses before, such that the Rx echoes in the figure are not referent to the Tx pulses shown.

to the F-Scan echo compression. The visualization of such maximization is depicted in Fig. 7, where the MIs are kept constant, the duty cycles are varied, and the acquisitions are checked for interferences.

From a timing perspective, duty cycles up to around 34% and 31% are feasible for the acquisition of the first and second swath, respectively. Such maximization is useful, as it can be used either to reduce the peak-to-average power ratio, or to increase the SNR. To visualize such a scenario, Fig. 8 depicts the transmitted and received signals in the time–frequency domain. Due to the system limitations, the duty cycles of the modes are limited to 30%. It can be noticed that little time is left unused due to the duty cycle optimization. Such a representation makes it possible to identify both the Tx and the nadir interference.

The steps taken in the selection of the timings for concurrent acquisitions with F-Scan are summarized in the flowchart depicted in Fig. 9. The range and the azimuth ambiguity-to-signal ratios (RASR/AASR) are used to define lower and upper limits, respectively, for the span of the MIs investigated. On the

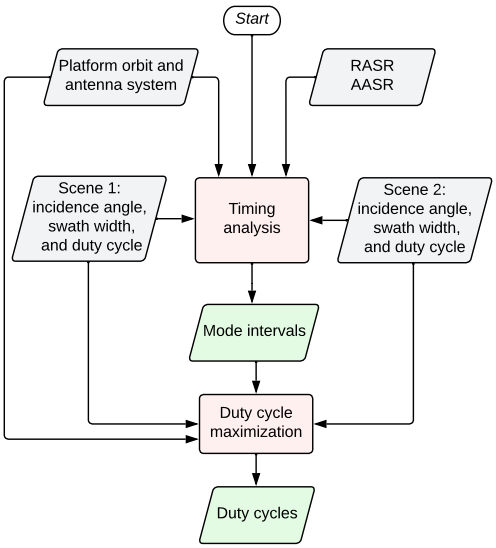

Fig. 9. Flowchart summarizing the steps taken to select proper MIs and duty cycles for a concurrent imaging acquisition with F-Scan.

one hand, it was observed that range ambiguities tend not to be an issue with the given high-gain pencil-beam antenna and the swath widths investigated. On the other hand, the concurrent aspect leads to a reduced effective PRF, causing azimuth ambiguities to be the main constraint. This restriction motivated limiting the lowest effective PRF to 2370 Hz. The assessment of such performance parameters is described in more detail in the following section.

III. Performance Assessment

The previously presented timing selection is the first step in the design of the concurrent F-Scan acquisition. This analysis typically leads to not only one possible MI combination but, as depicted in Fig. 6, to a collection. The imaging performance must be investigated among the possibilities to optimize the acquisition for the highest performance. Even if only one possibility is available, the performance must be checked to ensure sufficient imaging quality. This section derives the main performance parameters relevant to the novel imaging mode.

A. Azimuth Performance

The azimuth ambiguity performance and resolution are parameters influenced directly by the azimuth sampling rate. In the case of concurrent imaging, this rate is defined by the effective PRF. For the SM mode, the data can be processed with a lower azimuth bandwidth to improve the ambiguity performance at the cost of azimuth resolution. The ratio between the effective PRF and the azimuth processed bandwidth B_p is the azimuth oversampling factor given by

$$\alpha_{\mathrm{os,a}} = \frac{\mathrm{PRF}_\mathrm{eff}}{B_\mathrm{p}}. \tag{8}$$

Then, assuming the correction for the antenna pattern to get a rectangular spectrum, followed by the application of a processing window to achieve the required sidelobe suppression, the azimuth resolution is calculated by

$$\delta_\mathrm{az} = \frac{0.886\, v_\mathrm{g}}{B_\mathrm{p}} \gamma_\mathrm{w,a} \tag{9}$$

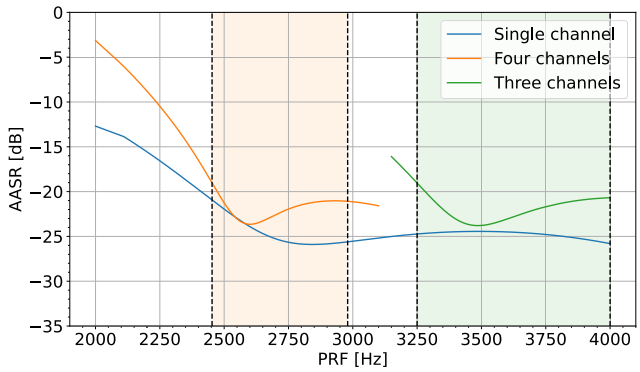

Fig. 10. Simulated AASR for the SM mode for the system described in Section II-C. A generalized Hamming window with $\alpha = 0.6$ m is considered. The x-axis represents the effective PRF in concurrent acquisitions. The blue curve depicts the AASR for the single-channel system, a processed bandwidth of 2110 Hz and a satellite speed of 7680 m/s. The orange curve shows the degraded AASR for the four-channel system with DPCA and a processed bandwidth of 8440 Hz, assuming the reconstruction method introduced in [34]. The green curve is relative to the three-channel case due to one overlapping virtual phase center and the same processed bandwidth of 8440 Hz. The highlighted areas are PRF limitations in which the AASR is kept lower than −19 dB and the noise scaling below 0.5 dB.

where v_g is the beam speed on ground and $\gamma_{w,a}$ is the broadening factor of the window applied in the processing step [3]. Such a window allows the improvement of the peak-to-sidelobe ratio (PSLR) and integrated sidelobe ratio (ISLR) of the impulse response at the expense of a degraded azimuth resolution. The window considered in this research is a generalized Hamming window with $\alpha = 0.6$ [3]. It enables, theoretically, the improvement of the PSLR from 13.2 dB to roughly 45 dB, but at the cost of a 32% degradation in resolution.

The AASR is a metric of how much aliasing is present in the Doppler spectrum. A higher effective PRF (sampling rate in azimuth) is desired, as it leads to a lower AASR and achieves finer azimuth resolutions. In concurrent imaging, high effective PRFs are challenging to obtain, as the sampling is shared between the modes, and a sufficient echo window length is required to fit the echoes from the swaths. For single-channel SM acquisitions, the AASR after the antenna pattern correction and the Hamming window is then estimated by

$$\mathrm{AASR} \approx \frac{\sum_{\substack{m=-\infty \\ m\neq 0}}^{\infty} \int_{-\frac{B_p}{2}}^{\frac{B_p}{2}} \frac{G_{az}^2(f_D + m\,\mathrm{PRF}_{eff})}{G_{az}^2(f_D)}\, W^2(f_D, B_p)\, \mathrm{d}f_D}{\int_{-\frac{B_p}{2}}^{\frac{B_p}{2}} W^2(f_D, B_p)\, \mathrm{d}f_D} \tag{10}$$

where G_{az} is the antenna one-way gain in azimuth [2], [6].

Equation (10) combined with the system parameters introduced in Section II-C leads to the blue curve in Fig. 10, where a processed bandwidth of 2110 Hz is considered. For multichannel systems, on the other hand, the AASR depends on the reconstruction method employed. For the technique introduced in [34], the AASR after reconstruction for both the three- and the four-channel cases are depicted by the orange and the green curves, respectively. The three-channel scenario is a consequence of the overlap of the virtual phase centers between consecutive PRIs due to the higher effective PRF.

B. Range Performance

1) Concurrent and F-Scan Considerations: The resolution in range is not directly affected by the concurrent aspect. F-Scan, in turn, intrinsically spreads the system bandwidth across the swath, thus affecting the range resolution. The effective bandwidth received by each target is directly related to the $\mathrm{HPBW_{el}}$ and the scene size. The total antenna scanning is given by $\beta_f - \beta_n$, as shown in Fig. 1, while each target is illuminated only by the angular extent of $\mathrm{HPBW_{el}}$. Therefore, similar to (3), the effective bandwidth is related to the total Tx bandwidth by

$$B_{eff} = \frac{\mathrm{HPBW_{el}}}{\beta_f - \beta_n} B_t. \tag{11}$$

The azimuth ambiguities assessment with concurrent F-Scan was shown to be similar to traditional SAR imaging. The assessment in range, however, is significantly different. The origin of the ambiguities is still the same, i.e., when both spurious and target echoes arrive at the antenna at the same time. Nevertheless, the concurrent and the F-Scan aspects lead to some specificities that change the RASR analysis.

First, the concurrent imaging aspect indicates the use of different antenna patterns in elevation for each mode and imaged area. The patterns point at scenes that can be very distant (100 km or more), so they cannot be approximated to be the same. As a consequence, two sorts of ambiguities appear: those spurious echoes that are transmitted and received by the same antenna pattern—denoted as same-mode range ambiguities—and those echoes that are transmitted and received by different antenna patterns—denoted as cross-mode range ambiguities. Moreover, the flexibility of having different MIs, duty cycles, and toggling up and down chirps for each mode shifts the positions of the ambiguities.

Concerning F-Scan, it implies that each point target in the scene is not imaged by a static (invariant in time and frequency) antenna pattern but by a sweeping one. Therefore, the assessment of the target echo's power and the ambiguous power is not as straightforward as in traditional imaging, where the antenna pattern in elevation is static for each point target. The approaches to account for each of these nuances in the range ambiguity assessment are described in this section. Numerical results for an exemplary acquisition are also presented.

2) Timing Determination of the Range Ambiguities: To visualize the locations of the ambiguities in a variable MI and duty cycle scenario with F-Scan, a time–frequency plot similar to the one presented in Fig. 8 is of great help. For this purpose, let us assume a concurrent F-Scan acquisition with two arbitrary modes named here, SM and ST, for clear nomenclature differentiation (the analysis procedure is the same for SM/SM and ST/ST). The waveforms considered are toggling up and down chirps. The objective is to understand and determine where the ambiguities for a given point target within one of the scenes are coming from. Assuming a point target A imaged with a center frequency f_A in SM mode, a simplified timing representation for this acquisition is presented in Fig. 11. The plot does not highlight the ST received echoes nor the rest of the SM targets, as these data

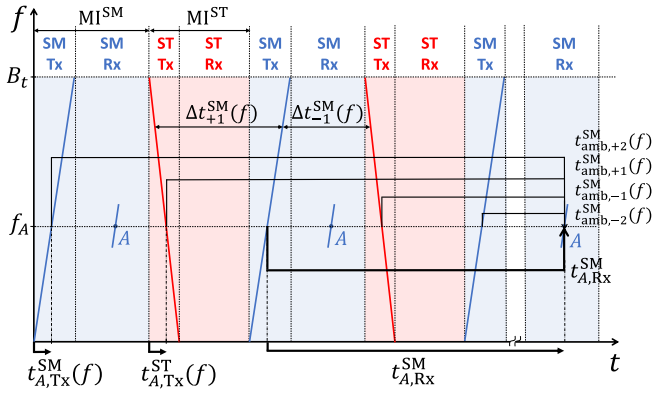

Fig. 11. Time–frequency plot for an exemplary concurrent F-Scan acquisition highlighting the first range ambiguities of the point target A. The objective of this representation is to facilitate the determination of the locations of the range ambiguities in a concurrent F-Scan scenario.

are not relevant to the desired objective of determining the positions of the ambiguities relative to the target A.

Range ambiguities occur when the echo of a point on the ground outside the scene (ambiguity) overlaps with the echo of a point target within the scene (target). Therefore, the ambiguity power in range arises from those echoes that arrive at the Rx antenna at the same time and with the same frequency as the main target. The ambiguity regions are point targets for the same-mode ambiguities—denoted hereafter as the even ambiguities—as they originate from every second pulse. On the other hand, the cross-mode ambiguities—also denoted as odd ambiguities—originate from an extended area, as the distance to the ambiguity varies with frequency due to the toggling chirps with different chirp rates. This frequency-variant behavior can be observed in Fig. 11, from which also the timings of the ambiguities relative to an arbitrary target A in the SM scene can be derived

$$\begin{cases} t^{\mathrm{SM}}_{\mathrm{amb},-2} = t^{\mathrm{SM}}_{A,\mathrm{Rx}} - \mathrm{PRI}_{\mathrm{eff}} & \text{(12a)} \\ t^{\mathrm{SM}}_{\mathrm{amb},-1}(f) = t^{\mathrm{SM}}_{A,\mathrm{Rx}} - \Delta t^{\mathrm{SM}}_{-1}(f) & \text{(12b)} \\ t^{\mathrm{SM}}_{\mathrm{amb},+1}(f) = t^{\mathrm{SM}}_{A,\mathrm{Rx}} + \Delta t^{\mathrm{SM}}_{+1}(f) & \text{(12c)} \\ t^{\mathrm{SM}}_{\mathrm{amb},+2} = t^{\mathrm{SM}}_{A,\mathrm{Rx}} + \mathrm{PRI}_{\mathrm{eff}} & \text{(12d)} \end{cases}$$

with

$$\begin{cases} \Delta t^{\mathrm{SM}}_{-1}(f) = \mathrm{MI}^{\mathrm{SM}} + t^{\mathrm{ST}}_{A,\mathrm{Tx}}(f) - t^{\mathrm{SM}}_{A,\mathrm{Tx}}(f) & \text{(13a)} \\ \Delta t^{\mathrm{SM}}_{+1}(f) = \mathrm{MI}^{\mathrm{ST}} - t^{\mathrm{ST}}_{A,\mathrm{Tx}}(f) + t^{\mathrm{SM}}_{A,\mathrm{Tx}}(f). & \text{(13b)} \end{cases}$$

The variable $t^{\mathrm{SM}}_{\mathrm{amb},k}(f)$ represents the echo delay of the ambiguity k, $t^{\mathrm{SM}}_{A,\mathrm{Rx}}$ the echo delay of the target A, and $t^{\mathrm{SM}}_{A,\mathrm{Tx}}(f)$ when within the Tx pulse the frequency f was transmitted. The above timings have to be checked for the frequency range equal to the bandwidth of the target A.

The echo delay of the ambiguities allows the determination of their positions on the ground. Combining the position information with the frequency, one can then assess the gain of the ambiguities both on Tx and Rx. The echo delay of the remaining ambiguities ($t_{\mathrm{amb},\pm3}$, $t_{\mathrm{amb},\pm4}$, etc.) can then be straightforwardly derived from the values obtained in (12) by shifts equal to the effective PRI. Naturally, the ambiguity timings still have to respect Earth's limits, such that points with echo delays lower than the nadir or higher than Earth's furthest line-of-sight delay are not considered.

Another possibility with the concurrent imaging is to receive, for instance, the SM echoes after an ST transmission, and vice versa. This inversion, fortunately, does not change the way the ambiguity positions are calculated.

3) RASR Formulation: Once the positions of the ambiguities are known, the next step is to calculate the power coming from the target and the ambiguities. Special care must be taken for cross-mode ambiguities, as the signals are transmitted with one pattern and received by a different one, i.e., one with a different phase shift and time delay configuration. Additionally, the antenna sweeping introduces a frequency-dependent gain, which is further affected by the antenna pattern correction and the processing window function. These latter steps are important to shape the spectrum of the range frequencies according to sidelobe suppression requirements. Here, the same Hamming window previously introduced is considered.

Due to the differences between the even and the odd ambiguities, it is useful to calculate the RASR as the sum of the contributions of both types of ambiguities

$$\mathrm{RASR} = \mathrm{RASR_e} + \mathrm{RASR_o}. \tag{14}$$

The RASR originating from the even ambiguities is very similar to traditional SAR imaging, and is given by

$$\mathrm{RASR_e} = \frac{\sum_{k=1}^{N} \frac{\sigma_{0,k}\,\overline{G}_k^2}{R_k^3 \sin\theta_{i,k}}}{\frac{\sigma_{0,0}\,\overline{G}_0^2}{R_0^3 \sin\theta_{i,0}}} \tag{15}$$

where σ_0 is the backscatter coefficient, θ_i the incidence angle, and $\overline{G}^2$ the average two-way gain. The subscripts 0 and k are references to the target and the kth ambiguity, respectively. The calculation of the average gain, given in (16), as shown at the bottom of the next page, accounts for the gain on Tx and Rx, the weight function, and the antenna pattern correction.

The calculation of the RASR for the odd ambiguities, on the other hand, considers the fact that the ambiguities are no longer point targets, but extended areas. The approach taken here is to average the contributions of the scatterers within these areas, which are effectively point targets for each instantaneous frequency. The equation for the $\mathrm{RASR_o}$ is given in (17), as shown at the bottom of the next page. In the final image, these ambiguities will be unfocused due to either the use of toggling chirps or just different chirp rates.

4) RASR Assessment: Finally, this RASR analysis can be extended and performed for any pair of MIs. From the timing analysis, it was shown that not every combination is suitable for the acquisition. Then, using the interference map obtained in Fig. 6(a), only the suitable MIs need to be investigated in terms of range ambiguities. For the ST acquisition, the calculated RASR values for the targets at far range are depicted in Fig. 12 as an example. The plot for the SM acquisition is similar but with better RASR values, as the SM scene is at a lower incidence angle.

Fig. 12 shows that RASR values between −35 and −43 dB can be achieved with a proper timing selection for the ST acquisition. The worst RASR obtained for the SM scene is at

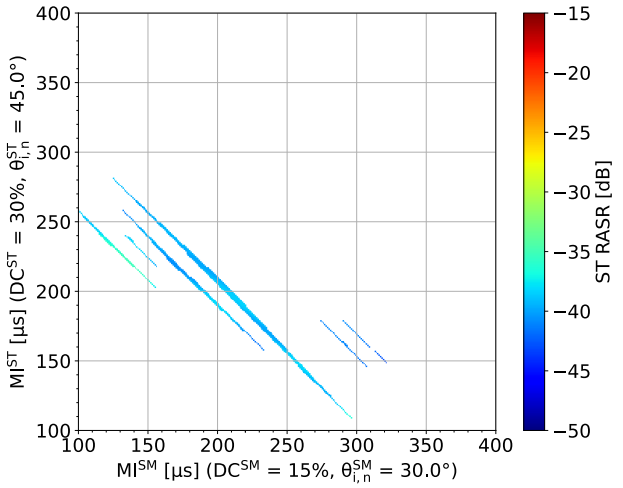

Fig. 12. ST RASR assessment as a function of the possible MI combinations for a concurrent SM/ST F-Scan acquisition. The RASR is calculated for the far range targets of the scene. The scenario considered is the same as in Fig. 6(a).

about −44 dB. Such good performance is a direct consequence of the pencil-beam antenna considered. Typically, ambiguities better than −20 dB are demanded [29], [39]. Therefore, the values achieved for this exemplary acquisition represent an excellent performance.

The scenario depicted here is only one particular example. To get a better picture of the overall performance of the designed mode, a global simulation must be performed as shown in Section IV.

C. Signal-to-Noise Ratio

An important parameter that facilitates the F-Scan analysis is the dwell factor (γ_w) introduced in [23]. It represents the factor observed both in (3) and (11), where the dwell time and the effective bandwidths were described. The dwell factor is given by

$$\gamma_w = \frac{\tau_{dwell}}{\tau_p} = \frac{B_{eff}}{B_t} = \frac{HPBW_{el}}{\beta_f - \beta_n}. \tag{18}$$

Additionally, it is useful for determining the power efficiency of the scanning. Fig. 1 shows that at the beginning and at the end of the scanning, the main lobe of the antenna pattern is pointing toward outside the scene to ensure a full sweep over the targets at the edges of the scene. This means that some energy is being wasted by not being transmitted to the scene. This loss is intrinsic to F-Scan and unavoidable. The parameter that nicely represents how much energy is transmitted outside the scene is the dwell factor. An approximation for the power loss is visualized in Fig. 13, where the antenna pattern is

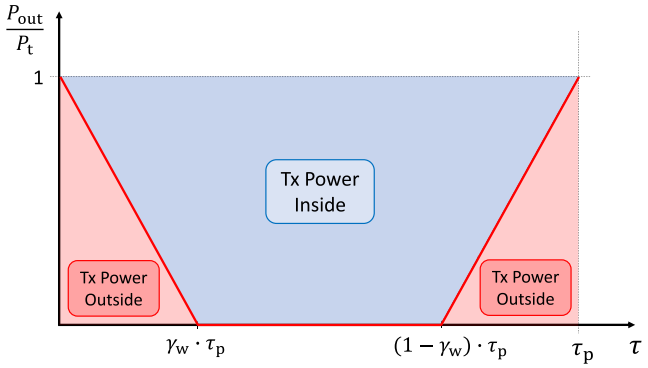

Fig. 13. F-Scan power transmitted to outside the scene (P_{out}) as a function of fast time during the Tx pulse. The antenna pattern in elevation is simplified to a rectangular window. The plot is normalized by the peak transmitted power (P_t). The dwell factor depicted in this figure is around 0.27.

simplified to a perfect rectangular window (constant gain within the HPBW, zero elsewhere).

The red line and the red areas in Fig. 13 depict how much of the total transmitted power and energy, respectively, are directed toward outside the scene during the pulse duration. The blue area, in turn, highlights the transmitted energy inside the scene. Dividing the red area by the total area, the portion of the total transmitted energy that is not contributing to the final processed scene equals to the dwell factor. In other words, F-Scan is more power efficient when the HPBW is small relative to the total scene angular size.

Proceeding with the power analysis of F-Scan, it is useful to compare how the SNR of a future system using F-Scan (such as the mission proposal HRWS) compares with the current state-of-the-art satellites using an SM mode (such as TSX).

First, one factor that significantly impacts the SNR, and strongly differs between current traditional and future F-Scan systems, is the antenna height. In traditional systems using the SM mode, the antenna height has to be sufficiently small to fit the whole target scene within the HPBW but large enough to avoid strong range ambiguities and ensure sufficient gain. Assuming an antenna size perfectly fitted to the swath width, its height is approximately given by $h_{ant}^{SM} \approx \lambda/(\beta_f^{SM} - \beta_n^{SM})$ [31].

In F-Scan, the angular size of the scene is related to the HPBW by the dwell factor as in (18). The antenna height of the F-Scan system is, therefore, given by

$$h_{ant}^{FS} = \frac{\lambda}{\beta_{f,eff}^{FS} - \beta_{n,eff}^{FS}} \frac{1-\gamma_w}{\gamma_w}. \tag{19}$$

F-Scan systems typically aim at scenes wider than the ones obtained with the traditional SM mode. Therefore, considering that the F-Scan scene is M_{SW} times wider than the SM one,

$$\overline{G}_k^2 = \frac{1}{B_{eff}} \int_{f_A - \frac{B_{eff}}{2}}^{f_A + \frac{B_{eff}}{2}} \frac{G^2(\beta_k, f)}{G^2(\beta_0, f)} W^2(f)\, df \tag{16}$$

$$RASR_o = \frac{\sum_{k=1}^{N} \frac{1}{B_{eff}} \int_{f_A - \frac{B_{eff}}{2}}^{f_A + \frac{B_{eff}}{2}} \frac{\sigma_{0,k}(\beta_k)\, G^{Tx}(\beta_k, f)\, G^{Rx}(\beta_k, f)}{R_k^3(\beta_k)\ \sin\theta_{i,k}(\beta_k)} \frac{W^2(f)}{G^2(\beta_0, f)}\, df}{\frac{\sigma_{0,0}\, \overline{G}_0^2}{R_0^3\ \sin\theta_{i,0}}}, \quad \text{with } \beta_k = \beta_k(f) \tag{17}$$

and assuming the same scene center, one can approximate $\beta^{\mathrm{FS}}_{\mathrm{f,eff}} - \beta^{\mathrm{FS}}_{\mathrm{n,eff}} \approx M_{\mathrm{SW}}\,(\beta^{\mathrm{SM}}_{\mathrm{f}} - \beta^{\mathrm{SM}}_{\mathrm{n}})$. The antenna heights of the two systems, therefore, are related by

$$\frac{h^{\mathrm{FS}}_{\mathrm{ant}}}{h^{\mathrm{SM}}_{\mathrm{ant}}} = \frac{1-\gamma_{\mathrm{w}}}{M_{\mathrm{SW}}\,\gamma_{\mathrm{w}}}. \tag{20}$$

The above factor is typically higher than one [29], [39]. A larger antenna increases the antenna gain and also comes along with the use of more T/R modules (TRMs), increasing the total Tx power. For instance, the German satellite TSX has an antenna with 384 TRMs and approximately 2 kW of radiated peak power [39]. The proposed mission HRWS, in turn, is planned to make use of 768 TRMs, achieving a peak power of approximately 7.7 kW [29]. Such an increase in the Tx power is made possible both by developments in TRM technology and also by the higher number of modules due to the larger antenna considered. Consequently, a linear increase in the antenna height leads to a cubic increase in the SNR—contribution of gain on Tx, gain on Rx, and higher Tx power.[1] Dividing the F-Scan and SM SNR expressions presented in [23], and disregarding the gain averaging of F-Scan due to the scanning and the losses at the edges of the SM scene due to the antenna pattern shape, one obtains

$$\frac{\mathrm{SNR}^{\mathrm{FS}}}{\mathrm{SNR}^{\mathrm{SM}}} = \frac{\left(\frac{P_{\mathrm{t}}\,A^2\,\gamma_{\mathrm{w}}}{B_{\mathrm{eff}}}\right)^{\mathrm{FS}}}{\left(\frac{P_{\mathrm{t}}\,A^2}{B_{\mathrm{t}}}\right)^{\mathrm{SM}}} = \left(\frac{h^{\mathrm{FS}}_{\mathrm{ant}}}{h^{\mathrm{SM}}_{\mathrm{ant}}}\right)^3 \frac{B^{\mathrm{SM}}_{\mathrm{t}}}{B^{\mathrm{FS}}_{\mathrm{t}}}. \tag{21}$$

The above formulation assumes the same duty cycles and antenna lengths for both systems.

Finally, the SNR improvement, or deterioration, of the F-Scan system relative to the SM one can be obtained by inserting (20) into (21)

$$\frac{\mathrm{SNR}^{\mathrm{FS}}}{\mathrm{SNR}^{\mathrm{SM}}} = \left(\frac{1-\gamma_{\mathrm{w}}}{M_{\mathrm{SW}}\,\gamma_{\mathrm{w}}}\right)^3 \frac{B^{\mathrm{SM}}_{\mathrm{t}}}{B^{\mathrm{FS}}_{\mathrm{t}}}. \tag{22}$$

Fig. 14 summarizes the above discussion, depicting the SNR difference between F-Scan and conventional SM as a function of the dwell factor for multiple values of M_{SW}. The total bandwidths of the F-Scan and SM systems are considered to be 1200 and 150 MHz, respectively. The black dotted lines are useful for visualizing the required relative increase of the F-Scan antenna size to achieve lower dwell factors and higher SNRs.

Comparing the F-Scan system described in Section II-C, which has an antenna height of 1.4 m, with TSX, which has an antenna height of 0.7 m, the SNR improvement is shown in Fig. 14 to be close to zero.

In terms of range resolution, however, a significant difference is observed between these two systems, which is highlighted by the blue curves on the right y-axis of Fig. 14. The concurrent imaging with F-Scan here described is foreseen to achieve swath widths of 25 km, leading to dwell factors between 0.3 and 0.5 (effective bandwidths between 360 and 600 MHz) for incidence angles from 20° to 50°. Consequently, the slant range resolution after the Hamming window and the correction for the antenna pattern stays between 50 and 30 cm: a significant improvement compared to the 1.2 m achieved with the 150 MHz of TSX, while maintaining similar NESZ performance.

An interesting property of F-Scan acquisitions is that the SNR does not vary significantly with the scene size. One could think that increasing the swath would lead to a lower effective duty cycle (dwell time) to each point target, thus deteriorating the SNR. At the same time, however, the effective bandwidth would also be reduced, thus improving the SNR. These two effects lead to a final SNR invariant with respect to the scene size. This characteristic is highlighted by the horizontal dashed lines in Fig. 14. Naturally, the drawback of increasing the scene size is a compromised range resolution.

The formulation above assumed the simplification of disregarding the gain averaging due to the F-Scan and also the losses at the edges of the main lobe for SM. Thus, the values derived are neither the worst nor the best case but rather an intermediate case comparison between the SNRs of the imaging techniques. However, the worst case, i.e., the worst NESZ of the scene, is a very important metric worth analyzing. For this purpose, these losses need to be taken into account. For SM, on the one hand, the maximum loss is strongly dependent on the incidence angle, antenna height, and swath width. On average, this loss sums up to −6 dB when the half-power beamwidth exactly fits the swath. For F-Scan, on the other hand, the scanning leads to a very advantageous property. Namely, as each point in the scene is scanned by the main lobe, the final NESZ is equalized and varies just slightly across the scene. Such averaging leads to a loss of about −1.6 dB. This parameter was previously described and named as the pulse extension loss in [23]. Hence, for the worst-case condition, F-Scan has a very significant SNR advantage over SM of about 4.4 dB.

Finally, the PRF of concurrent acquisitions has to be roughly doubled to preserve azimuth performance. Maintaining the same duty cycle, the Tx pulse duration is halved relative to a nonconcurrent acquisition. Consequently, the processing gain in range is also reduced by half, thus deteriorating the SNR by 3 dB. Alternatively, such an SNR loss can be seen as a consequence of the total transmitted energy being shared by the two generated images. Comparing the assumed system described in Section II-C to TSX, this loss is recovered by the 25% longer antenna in azimuth at the cost of an impaired azimuth resolution (the resolution is further improved by DPCA).

The following section presents the performance of the proposed concurrent F-Scan mode on a global scale.

IV. Global Performance

This section derives the previously analyzed performance parameters of the concurrent F-Scan mode on a global scale by means of a Monte Carlo simulation. The system parameters introduced in Section II-C are considered in conjunction with the LEO orbit of TSX [40], which maintains an altitude

[1] In this section, we assume a fixed total Tx bandwidth, thus the larger antenna would also lead to a deterioration of the range resolution. If the swath width and the range resolution were kept constant for different antenna heights, the SNR improvement would follow a quadratic increase instead, benefiting only from the increased Tx power and increased effective aperture on Rx.

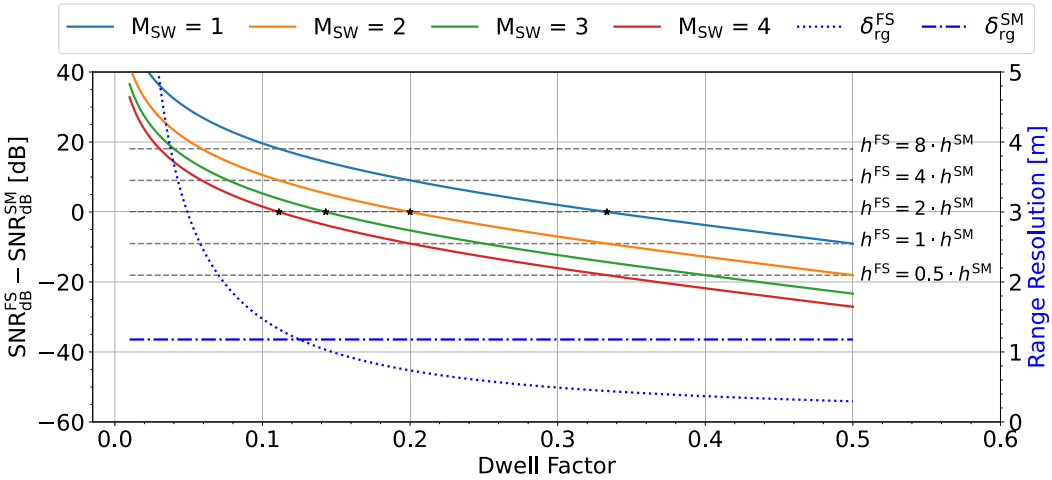

Fig. 14. SNR difference between F-Scan imaging and traditional SM as a function of the F-Scan dwell factor as obtained in (22) is illustrated on the left y-axis. The parameter M_{SW} indicates the swath width ratio between the F-Scan and the SM mode. Dashed black lines represent SNR differences for various ratios between the antenna heights of the F-Scan and the conventional SM systems as in (21). The total Tx bandwidth is assumed to be 1200 MHz for F-Scan, and 150 MHz for SM. The black asterisks highlight the intersection between the line referent to an F-Scan system with twice the antenna size of the SM and the SNR curves for different values of M_{SW}. The slant range resolutions are shown in blue on the right y-axis to highlight the trade-off between resolution and scene size for F-Scan imaging.

between 510 and 537 km over the WGS-84 ellipsoid. The basic idea of the simulation is to synthesize and analyze concurrent F-Scan acquisitions on a global scale. This global performance assessment allows for a better and more generalized understanding of the novel mode capabilities, avoiding, therefore, a potential misrepresentation from a specific pair of targets and acquisition geometry. The procedure described below was performed independently 10 000× to obtain a distribution representing the performance of the mode.

For this purpose, initially, a point target on the ground is selected following a uniform distribution in latitude and longitude, with a maximum absolute latitude of 70° due to the inclination of the orbit. Then, a second point target at the same latitude is obtained by a simple distance offset from the first target. The distance between the targets is randomized from a uniform distribution between 80 and 350 km. The positions of the targets are subsequently adjusted to align them in range, as offsets in azimuth are not relevant. This holds because targets at different azimuth positions do not require concurrent imaging but simply two different acquisitions at different moments in time. On the one hand, the lower limit of 80 km was chosen as targets within this distance do not require concurrent imaging, as F-Scan scenes of up to 80 km are already foreseen. On the other hand, the upper limit comes from the fact that distances higher than 350 km often lead to targets outside the desired incidence angle range of 20°–60°.

A further requirement for the simulated scenes is the swath width. For the results presented in this section, 25 km scenes—in ground range—are considered. Additionally, limits have to be defined on the allowed incidence angles to avoid strong degradation and distortion of the images. In this simulation, minimum and maximum incidence angles of 20° and 60° have been considered. These values are typical for data acquisitions with TSX [39]. Then, the full orbit is checked to find the satellite positions in which both targets appear within the access range.

For the pulse design, a minimum effective PRF of 2370 Hz paired with duty cycles of 15% and linear chirps are considered. The minimum PRF of 2370 Hz results in an AASR of about −19 dB as shown in Fig. 10. The MIs are limited to a minimum value of 65 μs, as lower values would not only lead to an insufficient echo window but also to a deterioration of the RASR.

Ultimately, for each pair of selected MIs, performance parameters are retrieved. Namely, azimuth and range ambiguities and resolutions are of great interest. The azimuth resolution is fixed to 4.0 m after the Hamming window, which means a processed bandwidth of about 2110 Hz, according to (9). The oversampling obtained is used to improve the AASR.

The performance of any mode is clearly not uniform globally. Depending on the latitude and the target positions relative to the satellite orbit, a different performance is achieved. This is especially true for concurrent F-Scan acquisitions, in which the extra degree of freedom, that is, the distance between the targets, makes each pair of targets unique. Therefore, due to this variance in performance between the randomized targets, 2-D histograms (density plots) are used to depict the performance in Sections IV-A and IV-B. These density heatmaps portray the results for both scenes and show a higher density of occurrences with colors shifted toward red, while blue represents fewer occurrences. All of the successful acquisitions are included in the histograms. Furthermore, the availability rate denotes the percentage of occurrences out of the 10 000 runs where a suitable MI selection was identified from a timing perspective.

Sections IV-A and IV-B present the results in two different scenarios: a single-channel system without DPCA, and a four-channel system with DPCA, respectively.

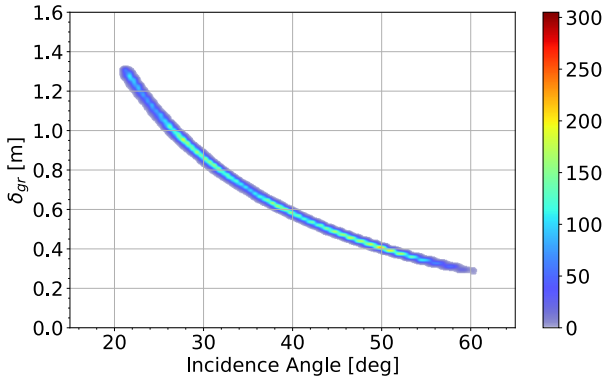

Fig. 15. Two-dimensional histogram of the ground range resolution as a function of the incidence angle of the scene center.

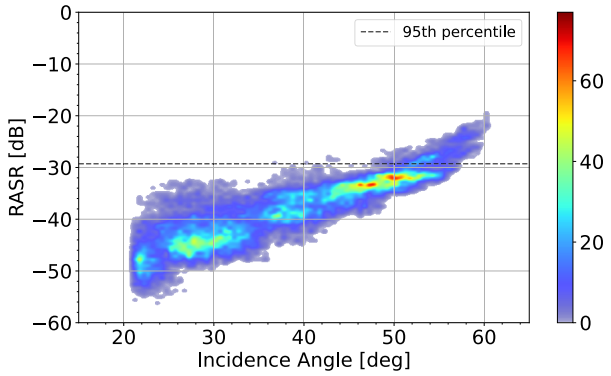

Fig. 16. Two-dimensional histogram of the RASR as a function of the incidence angle of the scene center.

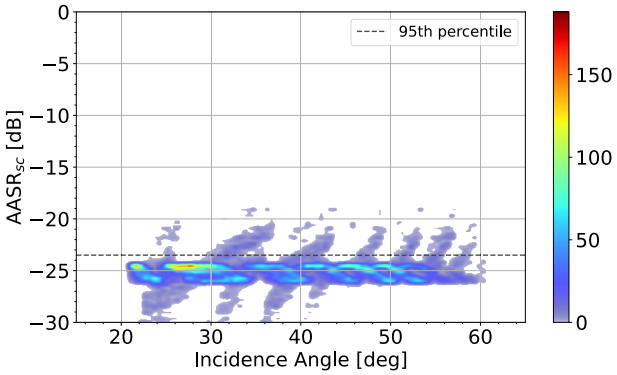

Fig. 17. Two-dimensional histogram of the AASR as a function of the effective PRF selected for the single-channel system.

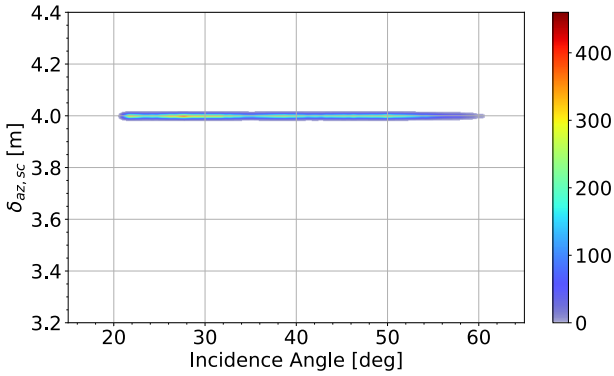

Fig. 18. Two-dimensional histogram of the azimuth resolution as a function of the incidence angle of the scene center for the single-channel system.

A. Single-Channel System

In each of the simulations, an important decision is the MI selection. It goes beyond determining the feasibility of the acquisition from a timing point of view, as, typically, multiple combinations are available due to the multiple approaches of the satellite to the scenes during its orbit. Due to the degraded azimuth performance from the concurrent aspect and excellent range ambiguity performance from F-Scan, the highest available effective PRF that can be used among all of the satellite's flyovers (opportunities of acquisition) is selected.

The ground range resolution is calculated directly from the effective bandwidth, the incidence angle of the scene center, and the processing window by

$$\delta_{\mathrm{gr}} = \frac{0.886\, c_0}{2\, B_{\mathrm{eff}}\, \sin\theta_{\mathrm{i}}}\, \gamma_{\mathrm{w,r}}. \tag{23}$$

The achieved ground range resolution is depicted in Fig. 15 as a function of the incidence angle of the scene center. The worst case is around 1.3 m for targets at 20°. At higher incidence angles, conversely, a higher effective bandwidth accompanied by a favorable slant-to-ground projection leads to a greatly improved resolution of about 0.3 m. The higher effective bandwidth is a consequence of the lower angle extension of the scenes at higher incidence angles, increasing the ratio displayed in (11).

In terms of ambiguity performance, the RASR as a function of the incidence angle is shown in Fig. 16. The incidence angle distribution of the targets is not uniform due to the possibility of acquiring from different geometries, i.e., different flyovers. As the simulation selects the orbit position leading to the highest effective PRF available, incidence angles near 60° are passed over in favor of steeper incidence angles. Targets between 55° and 60°, consequently, are not very often considered, as can be seen in the plot by the blue low-density area. A suitable parameter to define the RASR performance, therefore, is the 95th percentile, which reveals that in 95% of the acquisitions the RASR is below −29 dB—with a worst case of about −20 dB—representing excellent performance. The high dispersion of the RASR for a fixed incidence angle originates from the flexibility of the position of the other concurrent scene, which can be from 80 up to 350 km away, thus strongly affecting the cross-mode range ambiguities.

The AASR, as depicted in Figs. 10 and 17, stays below −23.5 dB for the effective PRFs higher than 2575 Hz, which accounts for 95% of the available acquisitions. For the remaining ones, a worst case of −19 dB is a consequence of needing to use a longer PRI to obtain the two 25 km swaths.

Finally, in terms of azimuth resolution, 4.0 m is achieved in all the acquisitions as shown in Fig. 18. This value is a direct consequence of the processed bandwidth and the processing window applied, which, in turn, are motivated by minimum AASR requirements.

The average worldwide availability obtained here for the scenario depicted is 97.3%. An acquisition is defined as available when—given the input requirements 25 km swath widths, scene positions, and minimum allowed effective PRF—there is an MI combination that respects the timing constraints. The remaining unavailable acquisitions can be made available by either reducing the scene size or, more conveniently, giving some flexibility to the exact positioning of the scenes.

TABLE II
SUMMARY OF THE PERFORMANCE IMPROVEMENTS OF THE CONCURRENT IMAGING MODE ACHIEVED WITH F-SCAN AND DPCA IN COMPARISON TO THE TRADITIONAL SM MODE

	Traditional Concurrent SM/SM (TerraSAR-X)	**Concurrent SM/SM with F-Scan (HRWS)**
Antenna size	0.7 m (El.) / 4.8 m (Az.)	1.4 m (El.) / 6.0 m (Az.)
Bandwidth	150 MHz	1200 MHz
Swath width	2x 15 km	2x 25 km
Distance (swaths)	30 - 250 km	80 - 350 km
Resolution (θ_i = 25°)	9.3 m^2	4.3 m^2 / 1.1 m^2 (DPCA)
Resolution (θ_i = 45°)	5.6 m^2	1.9 m^2 / 0.48 m^2 (DPCA)
RASR (95th perc.)	-19.6 dB	-29 dB
AASR (95th perc.)	-14.4 dB	-23.5 dB / -21 dB (DPCA)
Availability rate	72.5 %	97.3 % / 95.4 % (DPCA)

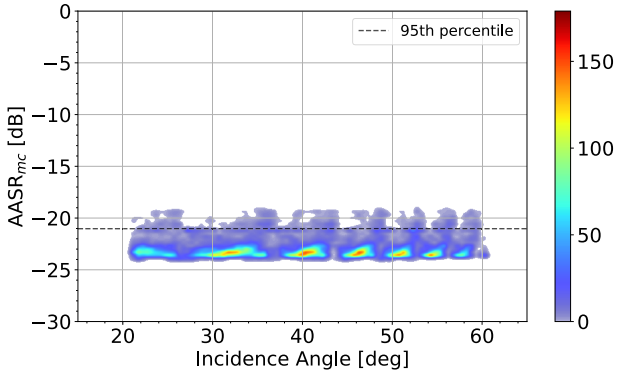

Fig. 19. Two-dimensional histogram of the reconstructed AASR as a function of the effective PRF used in the acquisitions for the multichannel system.

B. Multichannel System

By considering the multichannel capability of the system, which allows the use of DPCA, the azimuth resolution can be improved. An important constraint is, consequently, the allowed PRF interval. So as to avoid a strong degradation from the nonuniform sampling, according to Fig. 10, the effective PRF is limited to the highlighted areas, which are roughly from 2453 to 2980 Hz for the four-channel case, and from 3250 to 4000 Hz for the three-channel one. Such PRF intervals lead to a worst-case AASR of −19 dB and a maximum noise scaling of 0.5 dB. In the simulation, the effective PRF leading to the lowest error from the uniform sampling case is selected.

As DPCA is a technique in azimuth, the performance in range remains unchanged. In azimuth, on the other hand, the distribution of the AASR after reconstruction as a function of the incidence angle is depicted in Fig. 19, depicting a good 95th percentile of about −21 dB. As a consequence of the limited PRF intervals, the availability with DPCA drops to 95.4%. The azimuth resolution is improved by a factor of four, which is how much wider the antenna pattern of each individual channel in azimuth is compared to the entire antenna. Consequently, the azimuth resolution with DPCA is improved to 1.0 m. The reconstructed AASR can be improved by reducing the azimuth processed bandwidth, an acceptable compromise in light of the high azimuth resolution with DCPA.

C. Summary

The performance achieved by the novel imaging mode described in this article is summarized in the rightmost column of Table II. For comparison, the middle column depicts the concurrent imaging performance that can be achieved with a spaceborne state-of-the-art system without F-Scan, such as TSX. These results are refinements and adjustments of the preliminary results shown in [15].

From the results summarized in the table, it becomes clear that the performance is improved in every aspect. First, the maximum distance between the two concurrently imaged scenes can be increased due to the possibility of acquiring at higher incidence angles. This is a consequence of the improved range ambiguity performance brought by the F-Scan and the larger antenna. Besides, F-Scan also helps to increase the swath width by about 67% while also remarkably increasing the availability. Regarding resolution, the much higher bandwidth combined with DPCA leads to an up to tenfold improvement in the 2-D resolution. Finally, ambiguities, which were previously a concern for the conventional concurrent mode without F-Scan, now depict an excellent performance.

V. FURTHER OPTIMIZATION

The results obtained in this article represent an improvement compared to the original concurrent mode with TSX presented in [12] and [14]. For completeness and further improvements, some points still can be investigated.

First, the cross-mode nadir interference was considered not harmful to the final image due to the possibility of using

waveform encoding techniques to eliminate it, as demonstrated in [37] and [38]. A more comprehensive investigation of these possibilities alongside the F-Scan and the concurrent mode is then highly valuable.

Second, a more detailed discussion on the trade-offs between using F-Scan and simply the conventional SM mode is also of interest. This is especially the case for high-incidence angle imaging, where the angular target scene extent is roughly similar to the antenna HPBW in elevation. Therefore, it may not be worth using F-Scan in these situations, as plenty of energy is transmitted toward outside the target scene. This decision involves analyzing the trade-offs between the parameters of interest in these edge case scenarios, such as NESZ, swath width, and range resolution.

Additionally, to make available a broader PRF range to use with DPCA, one could also investigate a PRF-specific adaptation of the phase spoiling of the azimuth Tx pattern to obtain for each PRF a good compromise among azimuth ambiguities, noise scaling, and azimuth resolution.

Finally, concerning repeat-pass interferometric applications, special care regarding spectral decorrelation due to F-Scan would be required. Given that each target is imaged with a fraction of the total Tx bandwidth, an across-track baseline between the two acquisitions would lead to a shift in the bandwidth for each target. This effect needs to be added to the well-known baseline decorrelation [41] to ensure a common spectral support. A detailed investigation regarding the sensitivity to orbit deviations with F-Scan is the subject of future work.

VI. Conclusion

The concurrent imaging mode has the benefit of simultaneously obtaining two or more images, discarding the need to wait for the next flyover. F-Scan stands out as a solution to tackle the main challenges of the concurrent imaging mode, namely ambiguities and swath width. This article addressed in detail the procedures to design a concurrent F-Scan acquisition from a timing and performance perspective, especially in terms of swath width, ambiguity ratios, and resolution. The proposed approach is suitable for high-frequency SAR systems, for instance, in X- or Ka-band [30], [42]. Considering the parameters of the proposed German X-band mission HRWS, the concurrent imaging capabilities are shown to be significantly improved by F-Scan and DPCA. Namely, the scenes are wider, can be farther apart, have higher resolution,[2] and better ambiguity ratios, and are now vastly available. The excellent results pave the way for the operational implementation of such a concurrent technique on a global scale. The achieved performance improvement can be obtained with a purely analog or a hybrid (analog in elevation, digital in azimuth) beamforming system, which is more cost-effective than a fully DBF one. Additionally, implementing the proposed mode is expected not to introduce challenges in processing or additional hardware requirements. Thus, even though it is intended to serve as an auxiliary alternative in specific scenarios, the proposed concurrent mode with F-Scan can be considered a valuable tool in case of a real deployment.

[2]The larger antenna height needed for F-Scan leads actually to an immediate improvement of the SNR. Opportunely, the total Tx bandwidth can be increased to improve the range resolution, but at the cost of the aforementioned SNR improvement. The system presented here exploits this trade-off by using the 1.2 GHz bandwidth. As a result, the range resolution is improved as shown in Table II, and the SNR is only moderately improved as discussed in Section III-C.

Acknowledgment

The authors would like to express their appreciation to the anonymous reviewers for their insightful feedback, which significantly enhanced the quality of the article.

References

[1] W. G. Carrara, R. S. Goodman, and R. M. Majewski, *Spotlight Synthetic Aperture Radar*. Norwood, MA, USA: Artech House, 1995.

[2] J. Mittermayer, S. Wollstadt, P. Prats-Iraola, and R. Scheiber, "The TerraSAR-X staring spotlight mode concept," *IEEE Trans. Geosci. Remote Sens.*, vol. 52, no. 6, pp. 3695–3706, Jun. 2014.

[3] I. G. Cumming and F. H. Wong, *Digital Signal Processing of Synthetic Aperture Radar Data: Algorithms and Implementation*. Norwood, MA, USA: Artech House, 2005.

[4] F. De Zan and A. M. Guarnieri, "TOPSAR: Terrain observation by progressive scans," *IEEE Trans. Geosci. Remote Sens.*, vol. 44, no. 9, pp. 2352–2360, Sep. 2006.

[5] A. Meta, J. Mittermayer, P. Prats, R. Scheiber, and U. Steinbrecher, "TOPS imaging with TerraSAR-X: Mode design and performance analysis," *IEEE Trans. Geosci. Remote Sens.*, vol. 48, no. 2, pp. 759–769, Feb. 2010.

[6] J. Curlander and R. McDonough, *Synthetic Aperture Radar: Systems and Signal Processing*. New York, NY, USA: Wiley, 1991.

[7] ESA Communication Department. (Feb. 2014). *Bulletin Number 157*. Accessed: Apr. 20, 2021. [Online]. Available: https://esamultimedia.esa.int/multimedia/publications/ESA-Bulletin-157/offline/download.pdf

[8] S. D'Amico, C. Arbinger, M. Kirschner, and S. Campagnola, "Generation of an optimum target trajectory for the TerraSAR-X repeat observation satellite," in *Proc. 18th Int. Symp. Space Flight Dyn.*, Munich, Germany, 2004.

[9] S. Suri, L. Peterson, A. Kaptein, F. Cerezo, V. Moreno, and M. A. G. Primo, "TerraSAR-X/PAZ constellation: CONOPS, highlights and access solution," in *Proc. APSAR*, Singapore, 2015, pp. 178–183.

[10] D. Calabrese, V. Mastroddi, S. Federici, and S. Serva, "Discrete stepped strip (DI2S) for multi-swath acquisitions," in *Proc. IEEE 5th Asia–Pacific Conf. Synth. Aperture Radar (APSAR)*, Singapore, Sep. 2015, pp. 191–195.

[11] D. Calabrese, "Multiple-swath stripmap SAR imaging," U.S. Patent 9 869 764 B2, 2018. [Online]. Available: https://image-ppubs.uspto.gov/dirsearch-public/print/downloadPdf/9869764

[12] T. Kraus, J. P. T. Ribeiro, M. Bachmann, U. Steinbrecher, and C. Grigorov, "Concurrent imaging for TerraSAR-X: Wide-area imaging paired with high-resolution capabilities," *IEEE Trans. Geosci. Remote Sens.*, vol. 60, 2022, Art. no. 5220314.

[13] T. Kraus, J. P. T. Ribeiro, M. Bachmann, and R. Machado, "Ambiguity assessment and mitigation approaches for the TerraSAR-X concurrent imaging technique," in *Proc. EUSAR*. Leipzig, Germany: VDE, Jul. 2022, pp. 1–6.

[14] J. P. Turchetti Ribeiro, T. Kraus, M. Bachmann, and R. Machado, "Multiple PRI technique for concurrent imaging mode using TerraSAR-X," in *Proc. IEEE Radar Conf. (RadarConf22)*, New York City, NY, USA, Mar. 2022, pp. 1–6.

[15] J. P. Turchetti Ribeiro, T. Kraus, M. Bachmann, and R. Machado, "Introducing F-scan to the concurrent imaging mode," in *Proc. 24th Int. Radar Symp. (IRS)*, Berlin, Germany, May 2023, pp. 1–10.

[16] M. Younis, C. Fischer, and W. Wiesbeck, "Digital beamforming in SAR systems," *IEEE Trans. Geosci. Remote Sens.*, vol. 41, no. 7, pp. 1735–1739, Jul. 2003.

[17] G. Krieger, N. Gebert, and A. Moreira, "Multidimensional waveform encoding: A new digital beamforming technique for synthetic aperture radar remote sensing," *IEEE Trans. Geosci. Remote Sens.*, vol. 46, no. 1, pp. 31–46, Jan. 2008.

[18] A. Moreira et al., "Tandem-L: A highly innovative bistatic SAR mission for global observation of dynamic processes on the Earth's surface," *IEEE Geosci. Remote Sens. Mag.*, vol. 3, no. 2, pp. 8–23, Jun. 2015.

[19] A. Moreira, M. Zink, M. Bartusch, A. E. Nuncio Quiroz, and S. Stettner, "German spaceborne SAR missions," in *Proc. IEEE Radar Conf. (RadarConf)*, Atlanta, GA, USA, May 2021, pp. 1–6.

[20] C. Roemer, "Introduction to a new wide area SAR mode using the F-SCAN principle," in *Proc. IEEE Int. Geosci. Remote Sens. Symp. (IGARSS)*, Fort Worth, TX, USA, Jul. 2017, pp. 3844–3847.

[21] C. Roemer, R. Gierlich, J. Marquez-Martinez, and M. Notter, "Frequency scanning applied to wide area SAR imaging," in *Proc. EUSAR*. Aachen, Germany: VDE, Jun. 2018, pp. 1–5.

[22] C. Roemer, "High resolution wide swath synthetic aperture system," International Patent 2 019 015 911 A1, Jan. 24, 2019.

[23] M. Younis, F. Q. de Almeida, T. Bollian, M. Villano, G. Krieger, and A. Moreira, "A synthetic aperture radar imaging mode utilizing frequency scan for time-of-echo compression," *IEEE Trans. Geosci. Remote Sens.*, vol. 60, 2022, Art. no. 5239917.

[24] P. Guccione, D. Mapelli, D. Giudici, and A. R. Persico, "Design of f-SCAN acquisition mode for synthetic aperture radar," *Remote Sens.*, vol. 14, no. 20, p. 5283, Oct. 2022.

[25] L. Nan, G. Gai, T. Shiyang, and Z. Linrang, "Signal modeling and analysis for elevation frequency scanning HRWS SAR," *IEEE Trans. Geosci. Remote Sens.*, vol. 58, no. 9, pp. 6434–6450, Sep. 2020.

[26] Y. Liu et al., "A signal model based on the space–time coding array and a novel imaging method based on the hybrid correlation algorithm for F-SCAN SAR," *Remote Sens.*, vol. 15, no. 17, p. 4276, Aug. 2023.

[27] A. Currie and M. A. Brown, "Wide-swath SAR," *IEE Proc. F (Radar Signal Process.)*, vol. 139, no. 2, pp. 122–135, Apr. 1992.

[28] M. Bartusch, C. Bruens, A. E. Nuncio Quiroz, and S. Stettner, "HRWS: The upcoming German X-band spaceborne SAR mission," in *Proc. EUSAR*. Berlin, Germany: VDE, Mar./Apr. 2021, pp. 1–4.

[29] J. Mittermayer et al., "MirrorSAR: An HRWS add-on for single-pass multi-baseline SAR interferometry," *IEEE Trans. Geosci. Remote Sens.*, vol. 60, 2022, Art. no. 5224018.

[30] M. Bartusch, A. E. N. Quiroz, S. Stettner, A. Moreira, and M. Zink, "German X-band spaceborne SAR heritage and the future HRWS mission," in *Proc. IEEE Int. Geosci. Remote Sens. Symp. IGARSS*, Brussels, Belgium, Jul. 2021, pp. 804–807.

[31] C. A. Balanis, *Antenna Theory: Analysis and Design*, 4th ed. Hoboken, NJ, USA: Wiley, 2016.

[32] R. Scheiber, M. Martone, and N. Gollin, "Chirp selection and data compression for spaceborne wide-swath SAR in FScan-mode," in *Proc. EUSAR*, Mar./Apr. 2021, pp. 1–6.

[33] N. Gebert, G. Krieger, and A. Moreira, "Digital beamforming on receive: Techniques and optimization strategies for high-resolution wide-swath SAR imaging," *IEEE Trans. Aerosp. Electron. Syst.*, vol. 45, no. 2, pp. 564–592, Apr. 2009.

[34] G. Krieger, N. Gebert, and A. Moreira, "Unambiguous SAR signal reconstruction from nonuniform displaced phase center sampling," *IEEE Geosci. Remote Sens. Lett.*, vol. 1, no. 4, pp. 260–264, Oct. 2004.

[35] S. Wollstadt and J. Mittermayer, "Nadir margins in TerraSAR-X timing commanding," in *Proc. Committee Earth Observ. Satell. (CEOS)*, 2008, p. 4.

[36] J. Balkoski and F. Bordoni, "Nadir echo properties, a study based on TerraSAR-X data," in *Proc. 20th Telecommun. Forum (TELFOR)*, Nov. 2012, pp. 420–423.

[37] M. Villano, G. Krieger, and A. Moreira, "Nadir echo removal in synthetic aperture radar via waveform diversity and dual-focus postprocessing," *IEEE Geosci. Remote Sens. Lett.*, vol. 15, no. 5, pp. 719–723, May 2018.

[38] S.-Y. Jeon, T. Kraus, U. Steinbrecher, G. Krieger, and M. Villano, "Experimental demonstration of nadir echo removal in SAR using waveform diversity and dual-focus postprocessing," *IEEE Geosci. Remote Sens. Lett.*, vol. 19, pp. 1–5, 2022.

[39] M. Eineder et al., "TerraSAR-X basic product specification document," DLR Public Document, Oberpfaffenhofen, Germany, TD-GS-PS-3302, Tech. Rep. 1.9, 2013. [Online]. Available: https://sss.terrasar-x.dlr.de/docs/TX-GS-DD-3302.pdf

[40] R. Kahle and S. D'Amico, "The TerraSAR-X precise orbit control—Concept and flight results," in *Proc. Int. Symp. Space Flight Dyn. (ISSFD)*, Laurel, MD, USA, May 2014, pp. 1–12.

[41] F. Gatelli, A. Monti Guamieri, F. Parizzi, P. Pasquali, C. Prati, and F. Rocca, "The wavenumber shift in SAR interferometry," *IEEE Trans. Geosci. Remote Sens.*, vol. 32, no. 4, pp. 855–865, Jul. 1994.

[42] I. Hajnsek et al., "The Ka-band interferometric radar mission proposal for cold environments—SKADI," in *Proc. ESA Living Planet Symp.*, Bonn, Germany, May 2022.

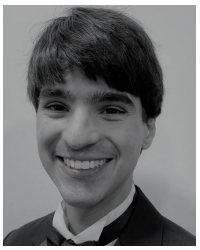

João Pedro Turchetti Ribeiro (Student Member, IEEE) received the B.S.E.E. and M.S.E.E. degrees from the Aeronautics Institute of Technology (ITA), São José dos Campos, Brazil, in 2021 and 2022, respectively. He is currently pursuing the Ph.D. degree with the German Aerospace Center (DLR), Weßling, Germany, and the Karlsruhe Institute of Technology (KIT), Karlsruhe, Germany.

His bachelor's thesis focused on developing a concurrent SAR imaging mode capable of performing two acquisitions simultaneously using the satellite TerraSAR-X. His master's thesis proposed further improvements to the concurrent mode through the F-Scan technique within the context of the mission proposal HRWS. Both theses were conducted in partnership with the Microwaves and Radar Institute, DLR. His main research interests include radar system performance, innovative SAR modes, and the development of high-resolution wide-swath SAR imaging techniques.

Mr. Turchetti Ribeiro was awarded second place in the Student Paper Award at the 15th European Conference on Synthetic Aperture Radar (EUSAR) held in Munich, Germany, for his work on multiple-swath SAR imaging with F-Scan, in 2024. His master's thesis was awarded the 2022 Prof. Cecchini Award for the best master's thesis of the year at ITA and secured third place in the ARGUS Science Award 2023 at Hensoldt.

Thomas Kraus received the M.Sc. degree in electrical engineering from the University of Ulm, Ulm, Germany, in 2009.

In 2010, he joined the Microwaves and Radar Institute, German Aerospace Center, Weßling, Germany, where he is currently working in the field of spaceborne SAR. He is involved in the instrument commanding, processing, and analysis of scientific and experimental acquisitions in the framework of the projects TerraSAR-X and TanDEM-X. He was responsible for the performance analysis during the operational implementation of the staring spotlight and the wide ScanSAR modes of TerraSAR-X as well as the dual receive antenna mode in the bistatic science phase of TanDEM-X. For the geostationary mission proposal Hydroterra, he also contributed the SAR performance analysis. His research interests include radar system performance, the development of innovative SAR modes, and the analysis of distributed satellite SAR systems.

Markus Bachmann received the Dipl.-Ing. and Ph.D. degrees in electrical engineering from the Technical University of Karlsruhe, Karlsruhe, Germany, in 2005 and 2015, respectively.

In 2005, he joined the Microwaves and Radar Institute, German Aerospace Center, Weßling, Germany. From 2005 to 2011, he was in charge of the implementation and calibration of the TerraSAR-X/TanDEM-X antenna model. From 2006 to 2010, he assessed the potentials and methods of the DEM calibration for TanDEM-X. From 2008 to 2010, he was responsible for the planning and execution of the TanDEM-X commissioning phase. From 2011 to 2014, he performed the interferometric and radargrammetric calibration of the TanDEM-X system and established the monitoring of the global coverage for the TanDEM-X mission. He has been the Head of the Mission Engineering Group, since 2012, which is in charge of the operational planning of the bistatic acquisitions for TanDEM-X and for future missions like Tandem-L, Rose-L Tandem, or HRWS, as well as for the analysis of mission relevant aspects in the frame of various SAR missions. He has been the Ground Segment Project Manager of the Tandem-L/Rose-L-Tandem Project, since 2016.

Renato Machado (Senior Member, IEEE) received the B.S.E.E. degree from São Paulo State University (UNESP), Ilha Solteira, São Paulo, Brazil, in 2001, and the M.Sc. and Ph.D. degrees in electrical engineering from the Federal University of Santa Catarina (UFSC), Florianópolis, Santa Catarina, Brazil, in 2004 and 2008, respectively.

From August 2006 to June 2007, he was a Visiting Ph.D. Scholar at the Department of Electrical Engineering, Arizona State University (ASU), Tempe, AZ, USA. From November 2013 to February 2015, he was a Visiting Research Fellow at Blekinge Institute of Technology (BTH), Karlskrona, Sweden, in partnership with Saab AB, Stockholm, Sweden. From August 2009 to December 2017, he was with the Federal University of Santa Maria, Santa Maria, Rio Grande do Sul, Brazil, where he was an Assistant Professor, from 2009 to 2016, an Associate Professor, in 2017, and lectured many courses in bachelor's and graduate programs and assumed different positions in the institution, namely, the Researcher Leader of the Communications and Signal Processing Research Group, the Coordinator of the Telecommunications Engineering Program, and the Director of the Aerospace Science Laboratory. Since December 2017, he has been an Associate Professor with the Aeronautics Institute of Technology (ITA), São José dos Campos, Brazil. He is the Research Leader of the Digital and Signal Processing Laboratory, ITA, and SAR and Radar Signal Processing Laboratory, ITA. He is a Principal Investigator of Brazilian Institute of Data Science (BI0S), Research Center for Applied Science and Technology in Artificial Intelligence—FAPESP/MCTI/CGI. From August 2021 to July 2022, he was the Head of the Graduate Program in Electronics and Computer Engineering, ITA. Since June 2022, he has been the Head of the Electronic Engineering Division, ITA. His research interests include SAR processing, SAR image processing, change detection, radar signal processing, digital signal processing, and AI signal processing.

Dr. Machado organized the XLI Brazilian Symposium on Telecommunications and Signal Processing, in 2023.

Gerhard Krieger (Fellow, IEEE) received the Dipl.-Ing. (M.S.) and Dr.-Ing. (Ph.D.) degrees (Hons.) in electrical and communication engineering from the Technical University of Munich, Munich, Germany, in 1992 and 1999, respectively.

From 1992 to 1999, he was with the Ludwig Maximilians University, Munich, where he conducted multidisciplinary research on neuronal modeling and nonlinear information processing in biological and technical vision systems. Since 1999, he has been with the Microwaves and Radar Institute, German Aerospace Center (DLR), Weßling, Germany, where he started as a Research Associate developing signal processing algorithms for a novel forward-looking radar system employing digital beamforming on receive. From 2001 to 2007, he led the New SAR Missions Group which pioneered the development of advanced bistatic and multistatic radar systems, such as TanDEM-X, as well as innovative multichannel SAR techniques and algorithms for high-resolution wide-swath SAR imaging. Since 2008, he has been the Head of the Radar Concepts Department which currently hosts about 60 scientists focusing on new SAR techniques, missions, and applications. He has been serving as a Mission Engineer for TanDEM-X and he also made major contributions to the development of the Tandem-L mission concept, where he led the Phase-0 and Phase-A studies. Since 2019, he also holds a professorship at the Friedrich-Alexander-University Erlangen, Erlangen, Germany. He has authored or coauthored more than 100 peer-reviewed journal papers, nine invited book chapters, about 500 conference papers, and more than 30 patents.

Prof. Krieger has been an Associate Editor of IEEE TRANSACTIONS ON GEOSCIENCE AND REMOTE SENSING, since 2012. From 2014 to 2024, he served as the Technical Program Chair for the European Conference on Synthetic Aperture Radar, and a Guest Editor for IEEE JOURNAL OF SELECTED TOPICS IN APPLIED EARTH OBSERVATIONS AND REMOTE SENSING in 2014. He received several national and international awards, including two Best Paper Awards at the European Conference on Synthetic Aperture Radar, two Transactions Prize Paper Awards of the IEEE Geoscience and Remote Sensing Society, and the W.R.G. Baker Prize Paper Award from the IEEE Board of Directors.

Alberto Moreira (Fellow, IEEE) received the bachelor's and master's degrees in electrical engineering from the Aeronautical Technological Institute (ITA), São José dos Campos, Brazil, in 1984 and 1986, respectively, and the Ph.D. degree (Hons.) from the Technical University of Munich, Munich, Germany, in 1993.

From 1996 to 2001, he was the Head of the Synthetic Aperture Radar (SAR) Technology Department, German Aerospace Center (DLR), Weßling, Germany. Under his leadership, the DLR airborne SAR system has been upgraded to operate in innovative imaging modes like polarimetric SAR interferometry, tomography, and holography. Since 2001, he has been the Director of the Microwaves and Radar Institute, DLR, and a Professor in the field of microwave remote sensing with Karlsruhe Institute of Technology (KIT), Karlsruhe, Germany. His DLR's Institute contributes to several scientific programs and projects for spaceborne SAR missions like TerraSAR-X, TanDEM-X, SAR-Lupe, and SARah, as well as Kompsat-6, PAZ, Sentinel-1, BIOMASS, ROSE-L, Harmony, Sentinel-1NG, Envision, and VERITAS. The mission TanDEM-X, led by his Institute, has generated a global, high-resolution digital elevation model of the Earth with unprecedented accuracy. He is the Initiator and the Principal Investigator (PI) for this mission. He has authored or coauthored more than 500 publications in international conferences and journals, eight book chapters, and holds more than 45 international patent grants in the radar and antenna field. His professional interests and research areas encompass spaceborne radar end-to-end system design, microwave techniques and system concepts, signal processing, and remote sensing applications.

Prof. Moreira was a member of the ESA Mission Advisory Groups of ENVISAT/ASAR, Sentinel-1, and Hydroterra, and currently is a member of the Science Study Team for the ESA's mission EnVision. He served as the President for the IEEE Geoscience and Remote Sensing Society (GRSS) in 2010, the General Co-Chair of IGARSS in 2012, and the General Chair of EUSAR in 2006. He was the Founder and the Chair of the GRSS German Chapter from 2003 to 2008. He has been serving as the Chair of the Major Awards of GRSS since 2017. He and his colleagues received the GRSS Transactions Prize Paper Awards in 1997, 2001, and 2007, and the GRSS Letters Prize Paper Award in 2015 and 2017. He is also a recipient of several international awards including the IEEE Aerospace and Electronic Systems Society (AESS) Fred Nathanson Award in 1999, the IEEE Kiyo Tomiyasu Technical Field Award in 2007, IEEE W.R.G. Baker Award from the IEEE Board of Directors in 2012, the IEEE GRSS Distinguished Achievement Award in 2014, and the IEEE Dennis J. Picard Medal for Radar Technologies and Applications in 2023. He served as an Associate Editor for IEEE GEOSCIENCE AND REMOTE SENSING LETTERS from 2003 to 2007 and has been serving for IEEE TRANSACTIONS ON GEOSCIENCE AND REMOTE SENSING since 2005.